DETECTION OF ENZYME ACTIVITY IN A PANCREATIC TUMOR MODEL USING CATALYCEST CONTRAST MRI

by

Anetta Goldsher

A Thesis Submitted to the Faculty of the

DEPARTMENT OF CHEMISTRY AND BIOCHEMISTRY

in Partial Fulfillment of the Requirements

for the Degree of

MASTER OF SCIENCE
WITH A MAJOR IN CHEMISTRY

In the Graduate College

THE UNIVERSITY OF ARIZONA

2017

STATEMENT BY AUTHOR

The thesis titled *Detection of Enzyme Activity in a Pancreatic Tumor Model Using CatalyCEST Contrast MRI* prepared by Anetta Goldsher has been submitted in partial fulfillment of requirements for a master's degree at the University of Arizona and is deposited in the University Library to be made available to borrowers under rules of the Library.

SIGNED: Anetta Goldsher

APPROVAL BY THESIS DIRECTOR

This thesis has been approved on the date shown below:

_____	8/4/2017
Mark D. Pagel	Date
Professor of Medical Imaging	
_____	8/4/2017
John C. Jewett	Date
Professor of Chemistry and Biochemistry	

ACKNOWLEDGEMENTS

I would like to thank first and foremost my advisor, Dr. Marty Pagel for his never-ending support. I would like to thank you for having faith in me and for always having the best metaphors. Thank you for being an excellent mentor and an even better teacher. Thank you for all your guidance and encouragement. I would have never been able to put all of this together without you.

I would like to thank my committee members for their insight. I would especially like to thank Dr. Amanda Baker, who was constantly aiding me in my project. Thank you for always being welcoming and supportive. I would like to thank Dr. Neale Hanke for all the cell work and *ex vivo* analysis. Thanks to Christy Howison for ordering the mice and performing the cell injections. A huge thank you to Gillian Paine-Murrieta for timely execution of drug injections and tumor excisions. A special thanks to Gabriela Fernandez-Cuervo for assisting in imaging and helping me with the hardest parts of animal work. Thank you so much to every CAMEL group member. In particular, thank you to Chathuri Kombala, Sam Gilmore, Alyssa Pollard, David Campbell, and Josh Goldenberg for aiding me in my projects and degree. I would like to thank Dr. Edward Randtke and Dr. Julio Cárdenas-Rodríguez for their assistance in the data processing. Also, thank you to the Mass Spectrometry and the Nuclear Magnetic Resonance Facilities for all their help in identification of compounds.

I would like to thank my friends in the Department of Chemistry and Biochemistry for taking time away from their research to help me address issues in my synthesis. In particular, thank you to David Smith for always being willing to help and for aiding me in compiling and editing my thesis. Additionally, thanks to Tristan Kleine, Michael Remesic,

and Billy Benson. A special thanks to the Polt group for allowing me to use their lyophilizer in time of need. I would like to thank the NIH for being the funding source for grant R01 CA169774.

I would like to thank my family for supporting me emotionally and at times, financially. Lastly and most importantly, I would like to thank my undergraduate student, Savannah Smith. Thank you for not only being the best lab worker but also my best friend. Thank you for all the late nights and weekends that you put in. I truly could not have done all of this without you.

Table of Contents

List of Figures

List of Schemes

List of Tables

List of Abbreviations

ABP	Activity-Based Probes
AIR	Assembly-Induced Retention
Bn	Benzyl group
Boc	*tert*-Butyloxycarbonyl group
BOP	benzotriazol-1-yloxy tris(dimethylamino)phosphonium hexafluorophosphate
BTZ	Bortezomib
CatalyCEST	Catalysis Chemical Exchange Saturation Transfer
Cbz	Carboxybenzyl group
CCD	Charge-Coupled Device
CEST	Chemical Exchange Saturation Transfer
DIACEST	Diamagnetic CEST
ESI	Electrospray Ionization
^{18}F-FDG	^{18}F-Fluorodeoxyglucose
FISP	Fast Imaging with Steady State Precession
FRET	Förster Resonance Energy Transfer
HATU	2-(7-Aza-1H-benzotriazole-1-yl)-1,1,3,3-tetramethyluronium hexafluorophosphate
HOAt	1-hydroxy-7-azabenzotriazole
HOBt	Hydroxybenzotriazole
HPLC	High Performance Liquid Chromatography
HRMS	High Resolution Mass Spectrometry
IκB	Inhibitor of κB

IV	Intravenous
LRMS	Low Resolution Mass Spectrometry
M	Molar
MRI	Magnetic Resonance Imaging
NF-κB	Nuclear Factor of κB
NIR	Near-Infrared
NMR	Nuclear Magnetic Resonance
PARACEST	Paramagnetic CEST
PBS	Phosphate Buffered Saline
PET	Positron Emission Tomography
QD	Quantum Dot
RF	Radio Frequency
ROI	Region of Interest
R_t	Retention Time
SPECT	Single Photon Emission Computed Tomography
T_1	Longitudinal relaxation time
T_2^*	Transverse relaxation time
TE	Echo Time
TFA	Trifluoroacetic Acid
TLC	Thin Layer Chromatography
TR	Repetition Time
uPA	urokinase Plasminogen Activator

Abstract

Detection of enzyme activity has gained popularity in molecular imaging because increased activity of enzymes such as urokinase plasminogen activator (uPA) can serve as biomarkers and assist in cancer diagnosis. Chemical exchange saturation transfer (CEST) Magnetic Resonance Imaging (MRI) is a non-invasive technique that can be utilized to detect enzyme activity; however, CEST MRI is not the only technique that can assess enzyme activity. Chapter 1 provides an overview of various imaging modalities that have been used to detect enzyme activity *in vivo*. Advances made in probe-design are discussed, in addition to advantages and disadvantages of each technique. Chapter 2 focuses on detection of uPA activity in a pancreatic cancer tumor model using a catalyCEST MRI contrast agent. Chapter 2 also discusses the importance of uPA in tumor biology, addresses the synthesis of the contrast agent, and evaluates the results of *in vivo* detection and *ex vivo* validation of uPA activity in response to therapy of pancreatic tumor models of Capan-2. The *in vivo* and *ex vivo* results showed no significant difference in uPA activity between chemotherapy-treated and non-treated mice. Additionally, no significant difference was observed between before and after chemotherapy-treated groups. Chapter 3 addresses some of the limitations of the study detailed in Chapter 2 and proposes improvements.

Chapter 1

ADVANCES IN THE FIELD OF MOLECULAR IMAGING FOR ENZYME DETECTION *IN VIVO*

1.1 Introduction

Enzyme activity detection is a way to look internally into biological and physiological processes. Abnormal enzyme activity can be a precursor for many human diseases.[1] Detecting enzyme activity *in vivo* can lead to faster and better diagnosis, and various imaging modalities can be used for this purpose. Each imaging technique has its own advantages and limitations. The techniques that will be discussed in this chapter include the following: optical imaging, magnetic resonance imaging, radionuclide imaging, and photoacoustic imaging.

1.2 Optical Imaging

Optical imaging is a method in which photons being emitted by fluorescent or bioluminescent probes are sensed by a detector. The advantage of using this method is high sensitivity.[2] The limitation of this imaging modality *in vivo* is the inability of light to travel from the agent to the detector through deeper tissue.[3] The signal from the probe can be scattered and absorbed by the tissue.[4] Also, the spatial resolution of this modality is low (1-2 mm).[5] These limitations make it difficult to detect enzyme activity below superficial tissue. Despite low penetration, much research has been done in the field of fluorescence and bioluminescence imaging.

1.2.1 Fluorescent Probes

Fluorescence imaging relies on the presence of fluorophore emitting light upon excitation.[6] When the fluorophore is excited by the appropriate wavelength of light, the emitted light of the shifted wavelength is detected by a charge-coupled device (CCD)

(**Figure 1.1**).[7] Signal can be achieved with two types of probes when trying to detect enzyme activity: always-on or activatable.

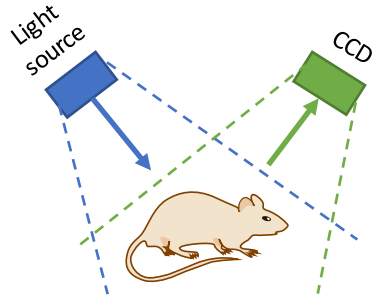

Figure 1.1. *Schematic illustration of a set up for fluorescence imaging.*

<u>Always-on and Activatable Probes</u>

Always-on and activatable probes produce florescence signal in different ways. Always-on probes are typically comprised of a fluorophore attached to an enzyme-targeting ligand. With a probe that is always fluorescent, signal at the site of the tumor depends on accumulation of enzyme-bound fluorophores and the excretion of non-bound fluorophores; the disappearance of non-bound fluorophores can take time (**Figure 1.2a**).[8] Studies have shown that signal specific to the tumor site can be detected 2-8 h after injection.[9] In addition to the long imaging time, the limitation of this probe is the lack of specificity for the enzyme activity, since the probe is always on regardless of its interaction with the enzyme of interest.

On the other hand, activatable probes only fluoresce in the presence of the desired enzyme (**Figure 1.2b**).[8] Thus, it is a faster and more specific approach. The focus of the rest of the optical imaging section will be on activatable probes unless stated otherwise. For the activatable probes, fluorescence can initially be suppressed until the desired catalytic

reaction has occurred. Two fluorescence-suppressing mechanisms, which are enzyme specific, will be discussed: capped and pre-quenched fluorophores.

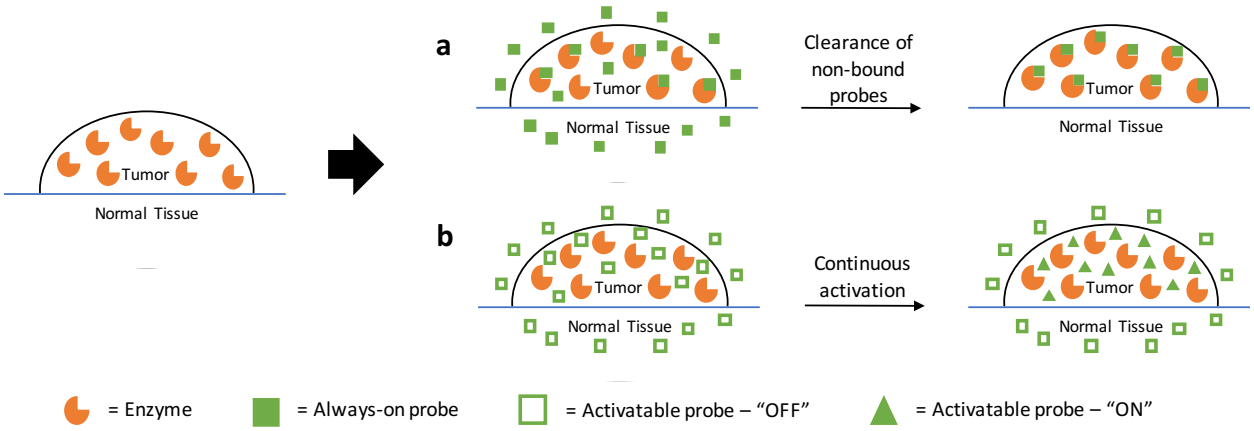

Figure 1.2. *Schematic illustration of two modes of signal generation for enzyme detection. The tumor expresses or over expresses an enzyme as opposed to the normal tissue. (a) Once the always-on probe is added, the probe binds to the enzyme, and time is allowed to pass for the clearance of non-bound probe. (b) Once the activatable probe is added, the enzyme activates the probe, and the fluorescence is recovered only at the site of the enzyme.*

Capped and Pre-Quenched Probes

Capped probes have a fluorophore that is directly attached to the enzyme substrate.[6] The fluorescence is quenched because it is bound to the substrate, but once the enzyme cleaves the substrate, the fluorescence is recovered.

Alternatively, pre-quenched probes have a fluorophore and a quencher attached by an enzyme-cleavable bond.[6] Once the enzyme cleaves the linker and releases the quencher, the fluorescence is recovered. The quenching of the fluorescence is caused by a phenomenon called Förster resonance energy transfer (FRET).[3] In FRET, the donor fluorophore is excited, but the energy is transferred to an acceptor, in this case, a quencher.[10] When the enzyme cleaves the linker between the fluorophore and the quencher, FRET is diminished as the quencher diffuses away from the fluorophore, so the photon is emitted from the fluorophore and can be detected (**Figure 1.3**).[11]

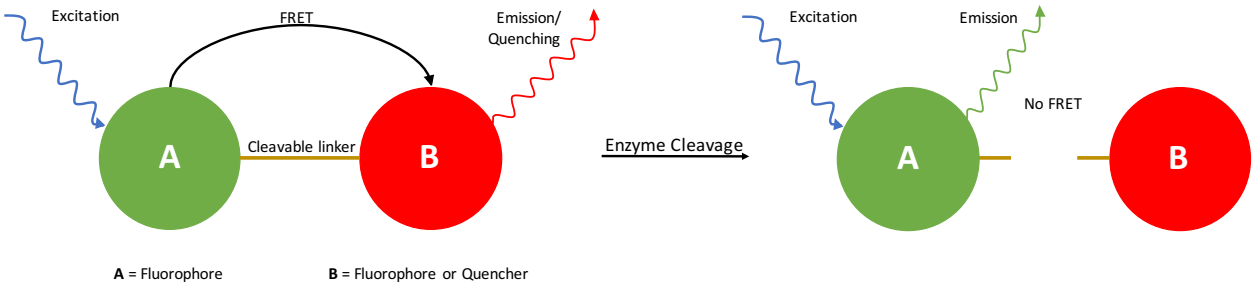

Figure 1.3. *Schematic illustration of enzymatic activation of fluorescent probes. Before the linker is cleaved, when fluorophore A is excited, the energy transferred to either another fluorophore, where it is emitted at a different wavelength, or a quencher. After enzyme cleavage, when fluorophore A is excited, it emits fluorescence at the respective wavelength.*

A variation of the fluorophore-quencher combination is fluorophore-fluorophore probe with a shifted wavelength (**Figure 1.3**). In this probe, a fluorophore is attached to another fluorophore by an enzyme-cleavable linker. Instead of the energy of the excited fluorophore being emitted at the wavelength of the donor for detection, it is relocated to the acceptor fluorophore, and the emission occurs at the frequency of the acceptor fluorophore. The acceptor fluorophore has an absorption spectrum that overlaps with the emission spectrum of the donor fluorophore. When the linker is cleaved, the absorption spectrum of the acceptor fluorophore shifts, allowing the emission spectrum of the donor fluorophore to be detected.[12]

Because of the shift in emission from fluorophore acceptor to fluorophore donor upon enzyme cleavage, FRET allows for ratiometric imaging to be used. Ratiometric imaging uses the ratio of two detected emission wavelengths to more quantitatively measure enzyme activity.[13] In the pre-quenched probe, the acceptor fluorophore has an emission at a certain wavelength, which is being monitored by a detector. The emission wavelength of the donor is also monitored. When the enzyme cleaves the linker between the two fluorophores, the intensity of the donor fluorophore increases as the intensity of

the conjugated probe decreases, and the ratio shows enzyme activity. This internal control allows for a more accurate detection of enzyme activity.

Despite advances like ratiometric imaging, fluorescence imaging still faces challenges of shallow tissue penetration and high background autofluorescence.[6] One way this issue is being addressed is by shifting the emission spectrum of the probes away from the visible light wavelengths closer to the infrared range.

Near-IR Fluorescent Probes

While *in vitro* work can be done with a full color spectrum, *in vivo* imaging has issues with shorter wavelength light because of absorption by hemoglobin and autofluorescence from tissue.[3] To by-pass this issue, near-infrared (NIR) probes have been developed and are being used. The NIR emission range is from 700 to 900 nm,[6] which allows the light to penetrate several centimeters.[14] The longer wavelength can be detected from deeper in the tissue than visible light and is the optimal range for a good balance between deeper tissue penetration and low autofluorescence.[15] However, the radiation at this wavelength can cause tissue heating, so care must be taken to use an appropriate intensity and duration of NIR light.[16] There are three major types of NIR probes: small molecules, nanomaterials, and polymers.

Small Molecules

Small molecule probes refer to lower molecular weight organic compounds. Small molecules make desirable probes because they exhibit fast distribution and activation (on the order of 30 minutes) and are excreted in a few hours.[3] This type of probe allows for imaging to be done closer to the injection time. In addition, fast excretion potentially reduces toxicity and shortens the imaging window.

Small molecule probes can be activated by enzymes in several ways. The probe can be capped and become fluorescent upon interacting with an enzyme.[17] This approach requires a change in the electronic properties of the molecule by an enzyme.[3] Alternatively, small molecule activity-based probes (ABP) can bind covalently to their enzyme targets, and the bond is usually irreversible.[3] ABPs can utilize either an always-on or activatable motif. For *in vivo* applications, it is more desirable for ABPs to have a quencher that is released upon binding with the enzyme.[3] Because of the irreversible binding, the ABPs are not excreted from the organism as quickly as their non-bound counterparts.

Lastly, small molecule probes can react with the enzymes of interest and self-assemble into nanostructures. Typically, the probe will have a protecting group that is cleaved by the enzyme and allows for the molecules to self-assemble.[18] The assembly of nanostructures allows for the fluorescence to be much brighter against the noise, making the enzyme activity easier to detect. Because this is a newer approach, only a few groups have demonstrated successful *in vivo* studies.[19] Even though self-assembly of small molecules into nanostructures is a relatively new field, there has been substantial work done with nanomaterial probes.

Nanomaterials

Due to the larger size, nanomaterial probes are able to produce much higher fluorescence; however, because of their size, these probes can take up to 24 hours to optimally accumulate at their target site and can take days to be excreted.[3] Quantum dots (QDs) are the most explored probes in the nanomaterial category for *in vivo* studies. Classical QDs use zinc(II), cadmium(II), selenide, and sulfide for the core and must be coated with an inert shell to avoid toxicity in cells.[20] However, QDs are not limited to those

four elements and can be synthesized from semiconductor materials from the elements of group II and VI or group III and V.[21-22] The advantages of using QDs over small molecule fluorophores include broadband excitation, narrow emission spectrum, large Stokes shifts, high quantum yields, and high resistance to photobleaching.[23] In addition to having large excitation and narrow emission bands, QDs can be tuned based on their shape and size to very specific wavelengths.[22] Lastly, QDs have a relatively long fluorescence lifetime.[24] For *in vivo* detection of enzyme activity, it has been shown that cleavable peptide chains with fluorescent dyes can be attached to QDs. The overlap of the excitation spectrum of the dye and emission spectrum of the QD allows for FRET to emit the QD signal until the dye is released from the QD by enzymatic cleavage of the peptide.[25] Alternatively, the dye on the peptide attached to the QD can have a quencher nearby, and once the dye is cleaved, then the fluorescence is recovered.[26] Despite the progress made in this field, there is room for exploration for the use of QDs for *in vivo* imaging of enzyme activity.

Polymers

Another way to increase fluorescence is to use polymers. Like QDs, polymers allow for attachment of many fluorophores on one molecule.[27] In particular, graft copolymers with an L-lysine backbone and enzyme-specific peptide with dye side-chain have been used to detect enzyme activity *in vivo.*[28] Because the dyes are in close proximity to each other, the fluorescence is self-quenched.[3] Upon cleavage by the enzyme, the dye is released, and the fluorescence is recovered (**Figure 1.4**). This field, much like the QDs, is still being explored, so as of now, *in vivo* data of enzyme activity using polymeric probes is limited.

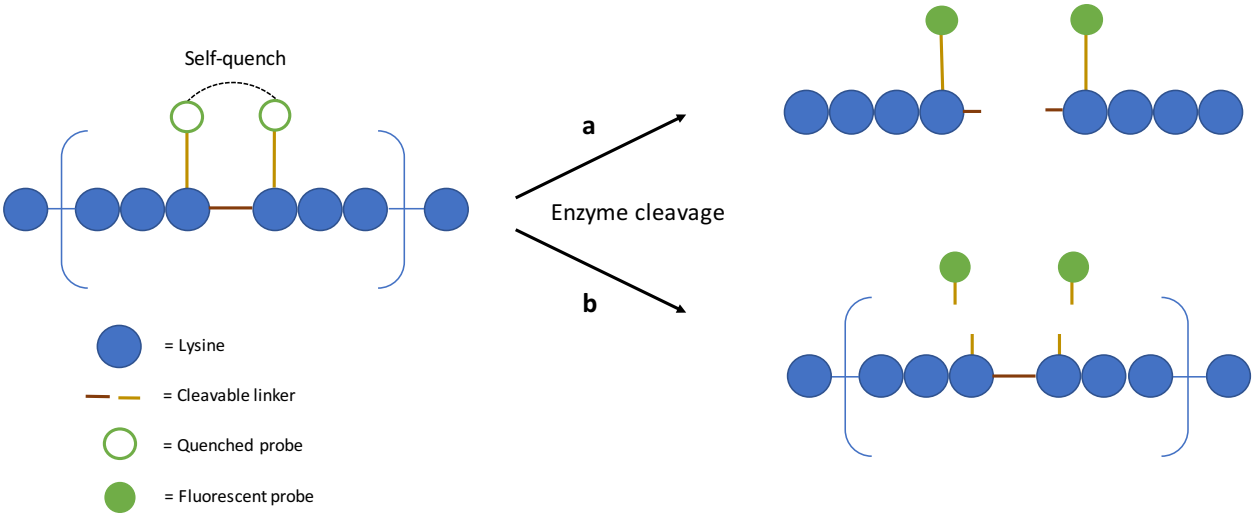

Figure 1.4. *Schematic illustration of poly-L-lysine type probes. The polymer chain has self-quenched fluorophores attached. (a) The fluorophore can be activated by cleavage of the main chain or (b) by cleavage of the side-chain.*

Conclusion for Fluorescence Imaging

Fluorescence imaging is a very sensitive imaging technique that uses probes, which are always-on or activatable. The quenching of activatable probes can occur though capping or pre-quenching. Pre-quenching is accomplished by the attachment of a quencher or another fluorophore though a FRET mechanism. The sensitivity of these probes comes with a price: depth of penetration and light scattering. To resolve these issues, NIR probes are used to maximize penetration and minimize interference from tissue due to autofluorescence. NIR probes are well suited for *in vivo* work, and thus a large amount of research has been investigated in this area. There are three categories of NIR probes: small molecule, nanomaterial, and polymer. The most commonly used and most explored probes are the small molecules. These probes have flexibility in their design for the target enzyme. However, the tunability of the fluorescence is limited because of the finite number of dyes that can be attached. On the other hand, less explored probes are nanomaterials. QDs can be fine-tuned to any emission wavelength and have a much higher quantum yield than

their small-molecule counterparts, which causes them to fluoresce much brighter. However, due to toxicity issues, QDs must be coated before they can be injected *in vivo*. Lastly, polymers allow for brighter fluorescence because of the number of dyes per molecule is much larger compared to small molecule probes. However, polymers have not been explored enough *in vivo* to make generalizations about the effectiveness and usefulness of these probes. Overall, fluorescence is a powerful and sensitive imaging modality but is limited to superficial locations and small animal work.

1.2.2 Bioluminescent Probes

Bioluminescence is a type of chemiluminescence that occurs naturally though the enzymatic oxidation of luciferins by luciferase to form oxyluciferin and emit a photon.[29] Because no outside excitation is needed (**Figure 1.5**), bioluminescence imaging does not suffer from high background noise due to autofluorescence of the tissues.[3] There are two methods to exploiting luciferase to detect enzyme activity *in vivo*: caging luciferin and caging luciferase.

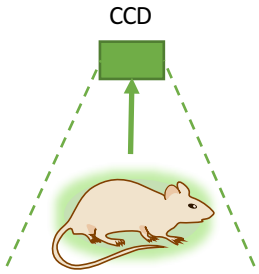

Figure 1.5. *Schematic illustration of a set up for bioluminescence imaging.*

Caged Luciferin Probes

One bioluminescence imaging method is to cage the substrate: luciferin. This is done by sterically hindering luciferin with an enzyme-cleavable side group.[3] Luciferase can only

oxidize luciferin once the target enzyme has cleaved the linker, so bioluminescence will only occur in the presence of the desired enzyme. However, because luciferase is not expressed in the animals that are being imaged, it must be encoded and expressed in the animals in the form of tumor xenografts or cell injections, or transgenic animals must be utilized.[3] To target different enzymes, a variety of side groups have been explored *in vivo*, such as peptides,[30] cephem,[31] and sugars.[32] Despite high sensitivity and success *in vivo*, the caged luciferase substrate modality is highly unfeasible for imaging patients because of the challenges of luciferase expression. Another approach to bioluminescence is to cage luciferase rather than the substrate.

Caged Luciferase Probes

Like caged luciferin probes, luciferase itself can be caged with an enzyme-cleavable linker **(Figure 1.6)**.[3] This type of imaging modality also requires the use of genetic modification, and several attempts have been successful *in vivo*. Luciferase has been modified to be connected between the N-terminus and the C-terminus by an enzyme-specific peptide linker **(Figure 1.6a)**.[33] Once the linker was cleaved, luciferase activity was restored, and bioluminescence was observed at the site of the enzyme of interest. In another variation, luciferase was modified to have a bulky group attached at the N-terminus and at the C-terminus by enzyme-specific cleavable peptide linkers **(Figure 1.6b)**.[34] Upon cleavage by the enzyme of interest, luciferase regained activity, and bioluminescence was observed. Caged luciferase probes are also not applicable in patients due to the genetic modification required in addition to the luciferin injection.

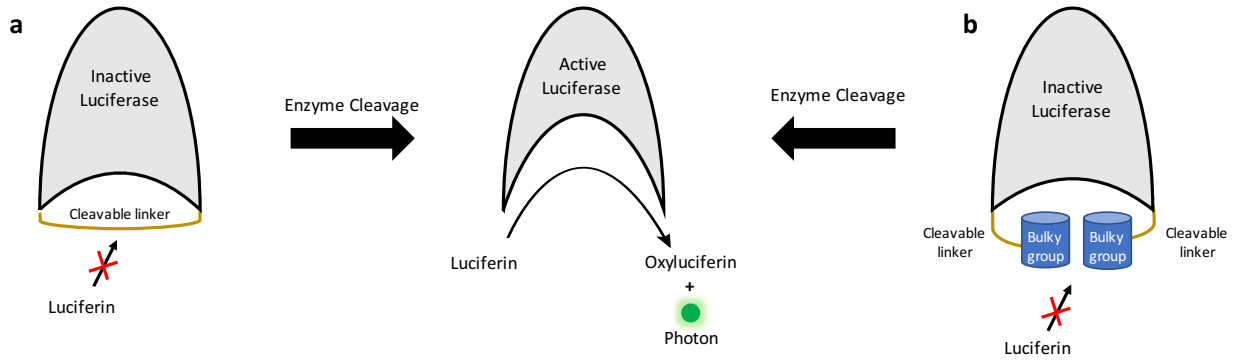

Figure 1.6. *Activation of caged luciferase. (a) Luciferase can be caged by binding the N-terminus to the C-terminus with a cleavable linker. Once the linker is cleaved, luciferase becomes active and oxidizes luciferin to oxyluciferin and emits a photon. (b) Luciferase can also be caged by binding bulky groups with cleavable linkers to the N-terminus and the C-terminus. Once the linkers are cleaved, luciferase becomes active and resumes its activity.*

Conclusion for Bioluminescence Imaging

Bioluminescence imaging allows for higher sensitivity than fluorescence imaging due to the lack of background noise. However, this imaging technique is highly dependent of the ability to genetically modify tissues in order to express luciferase. Without the ability to inject luciferase reliably, bioluminescence imaging remains impractical for clinical studies.

1.3 Magnetic Resonance Imaging

Magnetic resonance imaging (MRI) is a technique that uses a radio frequency (RF) pulse to orient the spin state of the net protons away from the magnetic field and then detects the time it takes for the nuclei to return to equilibrium.[35] MRI has a deep field of view and high spatial resolution but suffers from relatively poor sensitivity.[5] However, the low sensitivity can be compensated for by the high turnover rate of an enzyme, which allows for activated contrast agent to reach a detectable amount with an "agent-limited" approach.[36] This approach incorporates an excess of contrast agent that is irreversibly changed by enzyme catalysis and therefore starts accumulating near the enzyme of

interest. This approach is "agent-limited" because detection depends most on the amount of activated agent that is accumulated, rather than a "target-limited" approach that depends of the amount of enzyme target that is available.

1.3.1 T_1 MR Contrast Agents

The net magnetic vector of the protons in the sample is at thermal equilibrium when this vector is parallel to an external magnetic field. This net magnetic vector can be excited from its equilibrium state to be oriented perpendicular to the magnetic field. The excited net magnetic vector can relax back to equilibrium by two mechanisms. One of these mechanisms is longitudinal (T_1) relaxation. The T_1 relaxation time of water is shortened when Gd^{III} is present because of the interaction between the water molecules and Gd^{III} lanthanide metal ions, which attributes to a brighter image.[36] The interaction is dictated by the distance between the water proton and the Gd^{III} and by the rotational tumbling time of the Gd^{III} complex. The distance between the water proton and the Gd^{III} can be changed by blocking water access to the ion. Because Gd^{III} is usually chelated by organic compounds to reduce toxicity, these molecules provide a platform for enzyme activity detection through addition of substrates. A cleavable ligand can be attached to the Gd^{III} chelate, which blocks water accessibility. However, when the enzyme of interest removes the ligand, water accessibility is regained, and a shorter T_1 time is observed.[37] Another approach to detecting enzyme activity is to have an enzyme substrate attached to the chelate that upon cleavage can recruit and bind to a protein.[38-39] The bound protein slows down the rotational tumbling time of the agent and causes the T_1 time to decrease.

1.3.2 T_2* MR Contrast Agents

The other mechanism by which a change in the magnetic vector can be detected is by transverse (T_2^*) relaxation. Iron oxide can create a small, local magnetic field gradient, which alters the overall magnetic field for the water molecules in its proximity.[40] Because of this local magnetic field, the water molecules surrounding the iron oxide have range of MR frequencies.[36] The relaxation time that is measured is T_2^*, which is the dephasing process during the evolution of magnetism of water molecules at different frequencies that leaves no net coherent magnetization for detection.[41] The image is darker when the T_2^* relaxation time is decreased.[35] T_2^* is dependent on the strength of the superparamagnetism and the aggregation of the agent.[36]

Enzyme activity can be detected by changing the aggregation state of the agent. The iron oxide contrast agent can have a solubilizing linker, which upon cleavage by a target enzyme causes the nanoparticles to aggregate resulting in a decrease in T_2^* relaxation time.[42] Alternatively, the agent can have a linker that ties particles together, which upon cleavage by the desired enzyme causes the nanoparticle structure to degrade or dissociate leading to an increased T_2^* relaxation time.[43] For T_2 relaxation, the aggregation of the iron oxide nanoparticles can be controlled with cleavable linkers to detect enzyme activity.

1.3.3 CEST Contrast Agents

Chemical exchange saturation transfer (CEST) is an MRI contrast mechanism that reduces the signal of the bulk water after selective saturation at the frequency of an exchangeable proton on an MRI contrast agent.[40] Paramagnetic CEST (PARACEST) and diamagnetic CEST (DIACEST) agents can be used with this MRI mechanism. PARACEST

agents are metal chelates and have a large chemical shift from the water peak making them easier to detect. In comparison, DIACEST agents are metal-free organic molecules, which have a chemical shift within 10 ppm of the water peak. Either of these agents can be used to detect enzyme activity, which is termed "catalyCEST MRI".[36] The contrast agent can have an enzyme-cleavable ligand, and when it is cleaved, the CEST effect appears or disappears. However, depending on a lack of signal before or after cleavage can be unreliable, and therefore, an internal CEST effect must be utilized as a control.[36] The internal control allows for a ratiometric comparison, which is independent of the concentration of contrast agent.[44] PARACEST and DIACEST agents have been used to detect enzyme activity by the use of cleavable substrates.[45-46] Overall, CEST MRI allows for the detection of enzyme activity by monitoring the bulk water signal and seeing a change in the CEST effect after enzyme cleavage. Additionally, a ratiometric comparison allows for improved enzyme activity detection using this method.

1.3.4 Conclusion for MRI

MRI can be used to detect T_1 and T_2^* relaxation times, as well as the CEST effect. Even though MRI has relatively poor sensitivity, it has excellent spatial resolution and depth of penetration. The sensitivity can be compensated with the "agent-limited" approach, which relies on the fast turnover rate of the enzyme. With this approach, the sensitivity can be improved by increasing the amount of contrast agent. T_1 contrast agents rely on a toxic metal ion but provide a bright contrast. On the other hand, while iron oxide nanoparticles are less dangerous, T_2 contrast agents show a dark contrast, which may be difficult to distinguish from noise. Lastly, CEST provides an opportunity to image with DIACEST agents, which are much safer and use a ratiometric approach.

1.4 Radionuclide Imaging

Radionuclide imaging is a technique that relies on the decay of radioactive isotopes.[3] This type of imaging allows for high sensitivity (nM concentration) and high depth of penetration but low spatial resolution (1-2 mm).[5] The field is split into two categories depending on which isotope is being detected: single photon emission computed tomography (SPECT) and positron emission tomography (PET).

1.4.1 SPECT and PET

SPECT often uses the following common isotopes: ^{123}I, ^{99m}Tc, ^{111}In, and ^{67}Ga. Meanwhile, PET commonly uses ^{18}F, ^{11}C, ^{13}N, ^{15}O, ^{64}Cu, ^{76}Br, ^{124}I, and ^{68}Ga.[3] The radioactive isotopes for SPECT have a longer half-life than those of PET. The shorter half-life of the PET isotopes poses a problem in the timeliness of their synthesis and delivery.[3] Despite the short half-life, PET is a major imaging modality in oncology for patients.[48] In PET, decay of radioactive isotopes emits a positron that travels a short distance before it annihilates with an electron and releases two gamma rays in opposite directions, which are detected; meanwhile, SPECT detects a gamma ray that is emitted from the radioactive nucleus.[47] The detection of two gamma rays per radionuclide in PET allows for better spatial resolution relative to SPECT.[47] A widely used clinical probe for enzyme detection is ^{18}F-fluorodeoxyglucose (FDG), which is detected by PET.[49]

PET and SPECT imaging of enzyme activity can be done by relying on the principle that the enzyme-catalyzed product is trapped in cells.[3] This method works well for targeting enzymes like kinases. The addition of a charged, bulky group to the probe results in a molecule that cannot leave the cell as quickly as the non-reacted one.[50] The

congregated probes emit a stronger signal allowing for the enzyme activity to be detected. Alternatively, PET and SPECT probes can detect activity by binding to the desired enzyme. Typically, inhibitors are used as probes for this strategy to bind to the enzyme of interest and as a result can be detected due to their prolonged retention at the site of the enzyme.[51-52] However, even high affinity inhibitors give a short optimal imaging window.[52]

Even though PET and SPECT imaging provide high sensitivity and deep field of view, this imaging modality has rigorous time constraints due to the instability of the radioactive isotopes. In addition, the current strategies for detecting enzyme activity can only detect enzymes with very specific reactivity (binding of bulky groups) or have a very stringent imaging window. A better way to design diverse radionuclide probes must developed for this field to become more practical for enzyme detection.

1.5 Photoacoustic Imaging

Photoacoustic imaging is a relatively new technique.[53] In this technique, a short-pulsed laser is used to excite the molecule of interest. The excited molecules then undergo thermo-elastic expansion, which creates an acoustic signal that is detected by ultrasonic transducers surrounding the object.[54] The contrast of this technique comes with the sensitivity of optical imaging since the agent is excited with light, but the spatial resolution (~50 μm) comes with ultrasonic detection.[55] However, despite the high sensitivity and resolution, little work has been done with photoacoustic probes for enzyme detection *in vivo* because of the lack of an efficient approach for probe design.[6] One way to utilize photoacoustic imaging for enzyme activity is to use optical probes. Once the activatable optical probe is injected, the acoustic signal difference between the initial and cleaved

probe can be detected.[55-56] Alternatively, the aggregation of the small molecules into large nanomaterials after cleavage causes an assembly-induced retention (AIR) effect, which can synergistically enhance the photoacoustic contrast at the site.[57] These optical probes also have an enzyme-cleavable linker. When they are cleaved, the molecules are able to self-assemble into nanomaterials to produce an AIR effect with increased acoustic signal.[58-59] Despite these advances, the photoacoustic imaging field remains rather unexplored.

Photoacoustic imaging has the sensitivity that approaches optical imaging and very high spatial resolution in addition to good depth of penetration.[5] All these advantages make photoacoustic imaging a promising technique. However, more probes must be designed and tested *in vivo* to accelerate this field.

1.6 Conclusion

Detection of enzyme activity *in vivo* has gained significant interest in the molecular imaging field. The imaging modalities that have been explored for enzyme detection are optical imaging including fluorescence and bioluminescence, MRI, radionuclide imaging including SPECT and PET, and photoacoustic imaging, as summarized in **Table 1.1**. Optical imaging allows for high sensitivity but falls short with spatial resolution and depth of penetration. MRI allows for high spatial resolution and field of view but has low sensitivity. Radionuclide imaging has high sensitivity and field of view but has spatial resolution similar to optical imaging. Lastly, photoacoustic imaging has high sensitivity and spatial resolution but has average field of view. No single imaging modality is the optimal fit for detecting enzyme activity; however, the innovative approaches to imaging probe design

allows for the advantages of the imaging modalities to be exploited and limitations to be minimized.

	Optical Imaging	MRI	Radionuclide Imaging	Photoacoustic Imaging
Sensitivity	High	Average	High	High
Spatial Resolution	Low	High	Low	High
Depth of Penetration/ Field of View	Low	High	High	Average

Table 1.1. *Summary of advantages and limitations of discussed imaging techniques.*

1.7 References for Chapter 1

1. Baruch, A.; Jeffery, D. A.; Bogyo, M., Enzyme activity–it's all about image. *Trends in Cell Biology* **2004,** *14* (1), 29-35.

2. Kobayashi, H.; Choyke, P. L., Target-cancer-cell-specific activatable fluorescence imaging probes: rational design and *in vivo* applications. *Accounts of Chemical Research* **2010,** *44* (2), 83-90.

3. Razgulin, A.; Ma, N.; Rao, J., Strategies for *in vivo* imaging of enzyme activity: an overview and recent advances. *Chemical Society Reviews* **2011,** *40* (7), 4186-4216.

4. Kobayashi, H.; Ogawa, M.; Alford, R.; Choyke, P. L.; Urano, Y., New strategies for fluorescent probe design in medical diagnostic imaging. *Chemical Reviews* **2009,** *110* (5), 2620-2640.

5. Ntziachristos, V.; Razansky, D., Molecular imaging by means of multispectral optoacoustic tomography (MSOT). *Chemical Reviews* **2010,** *110* (5), 2783-2794.

6. Yan, R.; Ye, D., Molecular imaging of enzyme activity *in vivo* using activatable probes. *Science Bulletin* **2016,** *61* (21), 1672-1679.

7. Massoud, T. F.; Gambhir, S. S., Molecular imaging in living subjects: seeing fundamental biological processes in a new light. *Genes & Development* **2003,** *17* (5), 545-580.

8. Kamiya, M.; Urano, Y., Rapid and sensitive fluorescent imaging of tiny tumors *in vivo* and in clinical specimens. *Current Opinion in Chemical Biology* **2016,** *33*, 9-15.

9. Van Dam, G. M.; Themelis, G.; Crane, L. M.; Harlaar, N. J.; Pleijhuis, R. G.; Kelder, W.; Sarantopoulos, A.; De Jong, J. S.; Arts, H. J.; Van Der Zee, A. G., Intraoperative tumor-specific

fluorescence imaging in ovarian cancer by folate receptor-α targeting: first in-human results. *Nature Medicine* **2011,** *17* (10), 1315-1319.

10. Kikuchi, K., Design, synthesis and biological application of chemical probes for bio-imaging. *Chemical Society Reviews* **2010,** *39* (6), 2048-2053.

11. Jiang, S.; Win, K. Y.; Liu, S.; Teng, C. P.; Zheng, Y.; Han, M.-Y., Surface-functionalized nanoparticles for biosensing and imaging-guided therapeutics. *Nanoscale* **2013,** *5* (8), 3127-3148.

12. Lakowicz, J. R., Introduction to fluorescence. In *Principles of Fluorescence Spectroscopy*, Springer: 1999; pp 1-23.

13. Tsien, R.; Harootunian, A., Practical design criteria for a dynamic ratio imaging system. *Cell Calcium* **1990,** *11* (2-3), 93-109.

14. Ntziachristos, V.; Ripoll, J.; Weissleder, R., Would near-infrared fluorescence signals propagate through large human organs for clinical studies? *Optics Letters* **2002,** *27* (5), 333-335.

15. Ntziachristos, V.; Bremer, C.; Weissleder, R., Fluorescence imaging with near-infrared light: new technological advances that enable *in vivo* molecular imaging. *European Radiology* **2003,** *13* (1), 195-208.

16. Smith, K., *The Science of Photobiology*. Springer Science & Business Media: 2013.

17. Thorne, S. H.; Barak, Y.; Liang, W.; Bachmann, M. H.; Rao, J.; Contag, C. H.; Matin, A., CNOB/ChrR6, a new prodrug enzyme cancer chemotherapy. *Molecular Cancer Therapeutics* **2009,** *8* (2), 333-341.

18. Versluis, F.; van Esch, J. H.; Eelkema, R., Synthetic self‐assembled materials in biological environments. *Advanced Materials* **2016,** *28* (23), 4576-4592.

19. Ye, D.; Shuhendler, A. J.; Cui, L.; Tong, L.; Tee, S. S.; Tikhomirov, G.; Felsher, D. W.; Rao, J., Bioorthogonal cyclization-mediated *in situ* self-assembly of small-molecule probes for imaging caspase activity *in vivo*. *Nature Chemistry* **2014,** *6* (6), 519-526.

20. Wolfbeis, O. S., An overview of nanoparticles commonly used in fluorescent bioimaging. *Chemical Society Reviews* **2015,** *44* (14), 4743-4768.

21. Gao, X.; Yang, L.; Petros, J. A.; Marshall, F. F.; Simons, J. W.; Nie, S., *In vivo* molecular and cellular imaging with quantum dots. *Current Opinion in Biotechnology* **2005,** *16* (1), 63-72.

22. Michalet, X.; Pinaud, F.; Bentolila, L.; Tsay, J.; Doose, S.; Li, J.; Sundaresan, G.; Wu, A.; Gambhir, S.; Weiss, S., Quantum dots for live cells, *in vivo* imaging, and diagnostics. *Science* **2005,** *307* (5709), 538-544.

23. Rao, J.; Dragulescu-Andrasi, A.; Yao, H., Fluorescence imaging *in vivo*: recent advances. *Current Opinion in Biotechnology* **2007,** *18* (1), 17-25.

24. Frangioni, J. V., *In vivo* near-infrared fluorescence imaging. *Current Opinion in Chemical Biology* **2003,** *7* (5), 626-634.

25. Li, X.; Deng, D.; Xue, J.; Qu, L.; Achilefu, S.; Gu, Y., Quantum dots based molecular beacons for *in vitro* and *in vivo* detection of MMP-2 on tumor. *Biosensors and Bioelectronics* **2014,** *61*, 512-518.

26. Lee, S.; Ryu, J. H.; Park, K.; Lee, A.; Lee, S.-Y.; Youn, I.-C.; Ahn, C.-H.; Yoon, S. M.; Myung, S.-J.; Moon, D. H., Polymeric nanoparticle-based activatable near-infrared nanosensor for protease determination *in vivo*. *Nano Letters* **2009,** *9* (12), 4412-4416.

27. Weissleder, R.; Tung, C.-H.; Mahmood, U.; Bogdanov, A., *In vivo* imaging of tumors with protease-activated near-infrared fluorescent probes. *Nature Biotechnology* **1999,** *17* (4), 375-378.

28. Hsiao, J.-K.; Law, B.; Weissleder, R.; Tung, C.-H., *In-vivo* imaging of tumor associated urokinase-type plasminogen activator activity. *Journal of Biomedical Optics* **2006,** *11* (3), 034013-034013-5.

29. Thorne, N.; Inglese, J.; Auld, D. S., Illuminating insights into firefly luciferase and other bioluminescent reporters used in chemical biology. *Chemistry & Biology* **2010,** *17* (6), 646-657.

30. Dragulescu-Andrasi, A.; Liang, G.; Rao, J., *In vivo* bioluminescence imaging of furin activity in breast cancer cells using bioluminogenic substrates. *Bioconjugate Chemistry* **2009,** *20* (8), 1660-1666.

31. Yao, H.; So, M. K.; Rao, J., A bioluminogenic substrate for *in vivo* imaging of β‐lactamase activity. *Angewandte Chemie International Edition* **2007,** *46* (37), 7031-7034.

32. Wehrman, T. S.; von Degenfeld, G.; Krutzik, P. O.; Nolan, G. P.; Blau, H. M., Luminescent imaging of β-galactosidase activity in living subjects using sequential reporter-enzyme luminescence. *Nature Methods* **2006,** *3* (4), 295-301.

33. Kanno, A.; Yamanaka, Y.; Hirano, H.; Umezawa, Y.; Ozawa, T., Cyclic luciferase for real‐time sensing of caspase‐3 activities in living mammals. *Angewandte Chemie International Edition* **2007,** *46* (40), 7595-7599.

34. Laxman, B.; Hall, D. E.; Bhojani, M. S.; Hamstra, D. A.; Chenevert, T. L.; Ross, B. D.; Rehemtulla, A., Noninvasive real-time imaging of apoptosis. *Proceedings of the National Academy of Sciences USA* **2002,** *99* (26), 16551-16555.

35. Davies, G.-L.; Kramberger, I.; Davis, J. J., Environmentally responsive MRI contrast agents. *Chemical Communications* **2013,** *49* (84), 9704-9721.

36. Hingorani, D. V.; Yoo, B.; Bernstein, A. S.; Pagel, M. D., Detecting enzyme activities with exogenous MRI contrast agents. *Chemistry–A European Journal* **2014,** *20* (32), 9840-9850.

37. Louie, A. Y.; Hüber, M. M.; Ahrens, E. T.; Rothbächer, U.; Moats, R.; Jacobs, R. E.; Fraser, S. E.; Meade, T. J., *In vivo* visualization of gene expression using magnetic resonance imaging. *Nature Biotechnology* **2000,** *18* (3), 321-325.

38. Chang, Y.-T.; Cheng, C.-M.; Su, Y.-Z.; Lee, W.-T.; Hsu, J.-S.; Liu, G.-C.; Cheng, T.-L.; Wang, Y.-M., Synthesis and characterization of a new bioactivated paramagnetic gadolinium (III) complex [Gd (DOTA-FPG)(H2O)] for tracing gene expression. *Bioconjugate Chemistry* **2007,** *18* (6), 1716-1727.

39. Rodríguez, E.; Nilges, M.; Weissleder, R.; Chen, J. W., Activatable magnetic resonance imaging agents for myeloperoxidase sensing: mechanism of activation, stability, and toxicity. *Journal of the American Chemical Society* **2009,** *132* (1), 168-177.

40. Yoo, B.; Pagel, M. D., An overview of responsive MRI contrast agents for molecular imaging. *Frontiers in Bioscience: A Journal and Virtual Library* **2007,** *13*, 1733-1752.

41. Hingorani, D. V.; Bernstein, A. S.; Pagel, M. D., A review of responsive MRI contrast agents: 2005–2014. *Contrast Media & Molecular Imaging* **2015,** *10* (4), 245-265.

42. Granot, D.; Shapiro, E. M., Release activation of iron oxide nanoparticles:(REACTION) a novel environmentally sensitive MRI paradigm. *Magnetic Resonance in Medicine* **2011,** *65* (5), 1253-1259.

43. Colomb, J.; Louie, K.; Massia, S. P.; Bennett, K. M., Self‐degrading, MRI‐detectable hydrogel sensors with picomolar target sensitivity. *Magnetic Resonance in Medicine* **2010,** *64* (6), 1792-1799.

44. Hingorani, D. V.; Montano, L. A.; Randtke, E. A.; Lee, Y. S.; Cárdenas‐Rodríguez, J.; Pagel, M. D., A single diamagnetic catalyCEST MRI contrast agent that detects cathepsin B enzyme activity by using a ratio of two CEST signals. *Contrast Media & Molecular Imaging* **2016,** *11* (2), 130-138.

45. Sinharay, S.; Randtke, E. A.; Jones, K. M.; Howison, C. M.; Chambers, S. K.; Kobayashi, H.; Pagel, M. D., Noninvasive detection of enzyme activity in tumor models of human ovarian cancer using catalyCEST MRI. *Magnetic Resonance in Medicine* **2017,** *77* (5), 2005-2014.

46. Yoo, B.; Sheth, V. R.; Howison, C. M.; Douglas, M. J.; Pineda, C. T.; Maine, E. A.; Baker, A. F.; Pagel, M. D., Detection of *in vivo* enzyme activity with CatalyCEST MRI. *Magnetic Resonance in Medicine* **2014,** *71* (3), 1221-1230.

47. Ametamey, S. M.; Honer, M.; Schubiger, P. A., Molecular imaging with PET. *Chemical Reviews* **2008,** *108* (5), 1501-1516.

48. Couturier, O.; Luxen, A.; Chatal, J.-F.; Vuillez, J.-P.; Rigo, P.; Hustinx, R., Fluorinated tracers for imaging cancer with positron emission tomography. *European Journal of Nuclear Medicine and Molecular Imaging* **2004,** *31* (8), 1182-1206.

49. Smith, T., FDG uptake, tumour characteristics and response to therapy: a review. *Nuclear Medicine Communications* **1998,** *19* (2), 97-106.

50. Tjuvajev, J. G.; Finn, R.; Watanabe, K.; Joshi, R.; Oku, T.; Kennedy, J.; Beattie, B.; Koutcher, J.; Larson, S.; Blasberg, R. G., Noninvasive imaging of herpes virus thymidine

kinase gene transfer and expression: a potential method for monitoring clinical gene therapy. *Cancer Research* **1996,** *56* (18), 4087-4095.

51. Lee, K.-H.; Byun, S. S.; Choi, J. H.; Paik, J.-Y.; Choe, Y. S.; Kim, B.-T., Targeting of lacZ reporter gene expression with radioiodine-labelled phenylethyl-β-d-thiogalactopyranoside. *European Journal of Nuclear Medicine and Molecular Imaging* **2004,** *31* (3), 433-438.

52. Zhou, D.; Chu, W.; Rothfuss, J.; Zeng, C.; Xu, J.; Jones, L.; Welch, M. J.; Mach, R. H., Synthesis, radiolabeling, and *in vivo* evaluation of an 18F-labeled isatin analog for imaging caspase-3 activation in apoptosis. *Bioorganic & Medicinal Chemistry Letters* **2006,** *16* (19), 5041-5046.

53. Su, J. L.; Wang, B.; Wilson, K. E.; Bayer, C. L.; Chen, Y.-S.; Kim, S.; Homan, K. A.; Emelianov, S. Y., Advances in clinical and biomedical applications of photoacoustic imaging. *Expert Opinion on Medical Diagnostics* **2010,** *4* (6), 497-510.

54. Kim, C.; Favazza, C.; Wang, L. V., *In vivo* photoacoustic tomography of chemicals: high-resolution functional and molecular optical imaging at new depths. *Chemical Reviews* **2010,** *110* (5), 2756-2782.

55. Li, L.; Zemp, R. J.; Lungu, G.; Stoica, G.; Wang, L. V., Photoacoustic imaging of lacZ gene expression *in vivo*. *Journal of Biomedical Optics* **2007,** *12* (2), 020504-020504-3.

56. Levi, J.; Kothapalli, S. R.; Ma, T.-J.; Hartman, K.; Khuri-Yakub, B. T.; Gambhir, S. S., Design, synthesis, and imaging of an activatable photoacoustic probe. *Journal of the American Chemical Society* **2010,** *132* (32), 11264-11269.

57. Wang, L.; Yang, P.-P.; Zhao, X.-X.; Wang, H., Self-assembled nanomaterials for photoacoustic imaging. *Nanoscale* **2016,** *8* (5), 2488-2509.

58. Dragulescu-Andrasi, A.; Kothapalli, S.-R.; Tikhomirov, G. A.; Rao, J.; Gambhir, S. S., Activatable oligomerizable imaging agents for photoacoustic imaging of furin-like activity in living subjects. *Journal of the American Chemical Society* **2013,** *135* (30), 11015-11022.

59. Zhang, D.; Qi, G. B.; Zhao, Y. X.; Qiao, S. L.; Yang, C.; Wang, H., *In situ* formation of nanofibers from purpurin18‐peptide conjugates and the assembly induced retention effect in tumor sites. *Advanced Materials* **2015,** *27* (40), 6125-6130.

Chapter 2

DETECTION OF EARLY THERAPEUTIC RESPONSE BY MONITORING UROKINASE PLASMINOGEN ACTIVATOR ACTIVITY WITH CATALYCEST MRI

2.1. Introduction

2.1.1. Role of uPA in Tumor Biology

The nuclear factor (NF)-κB signaling pathway has been identified as one of the two important regulators of immunity and inflammation (**Figure 2.1**).[1] NF-κB remains inactive in the cell when it is bound to the inhibitor IκB; however, when IκB is phosphorylated, it is targeted for ubiquitination and degraded.[2] Once NF-κB is activated, it can bind to designated sites on the chromatin to allow for the transcription of genes necessary for immune and inflammatory response.

In the mammalian immune and inflammatory regulation, NF-κB regulates the expression of a wide variety of genes.[1] Pro-urokinase plasminogen activator (uPA) is one of the enzymes that is transcribed and translated as part of the NF-κB cascade.[3-4] Once pro-uPA is then excreted out of the cell, it can bind to the uPA receptor (uPAR), which converts the inactive pro-uPA to active uPA.[5] Active uPA can then go on to convert plasminogen into plasmin, which can degrade most extracellular proteins.[6] In normal tissue, plasmin allows for cell migration and tissue remodeling.[3] However, in cancer cells, the uPA pathways is used for invasion and metastasis.[6-7]

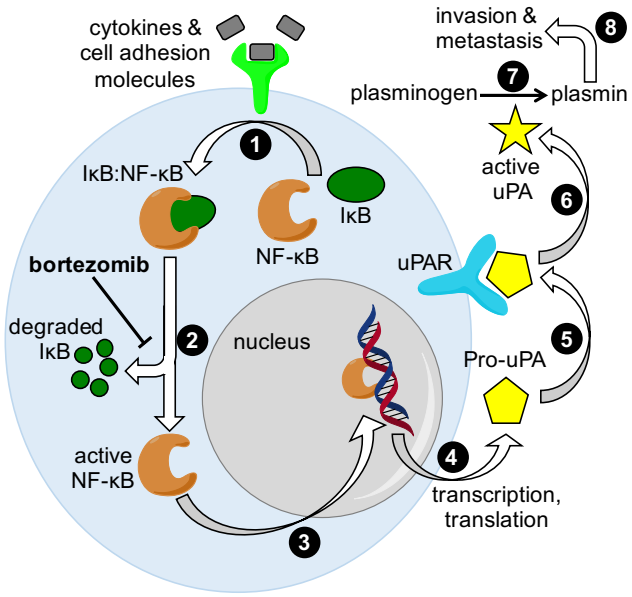

Figure 2.1. *Diagram of the NF-κB pathway, highlighting the expression, activation, and function of uPA and inhibition of this pathway by bortezomib. (1) NF-κB is signaled to bind IκB to remain inactive in the cell. (2) IκB is tagged with ubiquitin to be degraded. (3) Active NF-κB allows for the transcription and translation of pro-uPA. (4) Pro-uPA is excreted out of the cell and (5) binds to uPAR. (6) uPA is activated. (7) uPA catalyzes plasminogen into plasmin. (8) Plasmin allows for invasion and metastasis of cancer cells.*

Chemotherapy can be used intervene in the NF-κB pathway. Bortezomib (BTZ) is a proteasome inhibitor, which interferes with the degradation of IκB. If IκB is unable to be degraded, then NF-κB remains inactive, and pro-uPA cannot be transcribed and translated. Because the precursor is no longer available, the amount and activity of uPA is decreased, and plasminogen is not converted plasmin, which slows invasion and metastasis. Therefore, we hypothesized that a decrease in uPA activity can be observed after administration of BTZ.

2.1.2. CatalyCEST MRI to Detect uPA

The ability to detect uPA *in vivo* can potentially provide faster disease diagnosis, since overexpression of uPA is considered to be an important biomarker in breast,[8] lung,[9] bladder,[10] stomach,[11] colorectum,[12] cervix,[13] ovary,[14] kidney,[15] and brain cancers.[16]

CatalyCEST MRI can be used to detect uPA activity *in vivo*. In CEST MRI, specific protons on the contrast agent are saturated by an RF pulse (**Figure 2.2a,b**). The saturated proton can exchange with bulk water and decrease the water signal at that frequency

(**Figure 2.2c**). In catalyCEST MRI, the CEST signal disappears after enzyme catalysis (**Figure 2.2d**).[17] In this study, we proposed to use catalyCEST MRI to detect a therapeutic response by monitoring change in uPA activity *in vivo* using a mouse model of Capan-2 human pancreatic cancer.

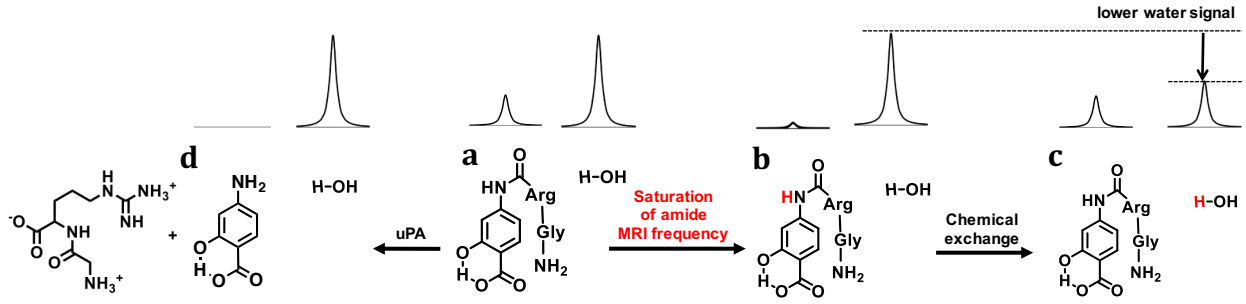

Figure 2.2. *Diagram of catalyCEST MRI. (a) The representative initial signals of the amide and water protons. (b) The amide proton is selectively saturated (shown in red), and the signal of the proton is diminished. (c) Once chemical exchange occurs between the amide group and the water molecule, the amide signal is regained, but the bulk water signal is decreased. (d) When uPA cleaves the peptide from the 4-aminosalicylic acid moiety, the water signal is regained, because the exchange of the free amine is too fast to generate CEST.*

2.2. Materials and Methods

2.2.1. Synthesis of Contrast Agent

All reactions were performed under an inert atmosphere of argon equipped with a magnetic stirrer using dry solvents unless otherwise indicated. Flash column chromatography was performed using silica gel (particle size 0.04-0.06 mm and 230-400 Å mesh size). An analytical HPLC system (Agilent Technologies, 1200 series) and a preparative HPLC system (Agilent Technologies, 1260 series) were used for analysis and purification. Reactions were monitored using thin layer chromatography (TLC) on silica gel plates (Sigma Aldrich). All other reagents were obtained commercially and used as received.

Physical measurements

^{1}H and ^{13}C NMR spectra were recorded with Bruker AVIII 400 MHz and DRX 500 and 600 MHz NMR instruments (Bruker Biospin, Inc., Billerica, MA). Low resolution mass spectra were collected with an Amazon Ion Trap instrument (Bruker Biospin, Inc., Billerica, MA), and high-resolution mass spectra were collected with a FT-ICR instrument (Bruker Biospin, Inc., Billerica, MA).

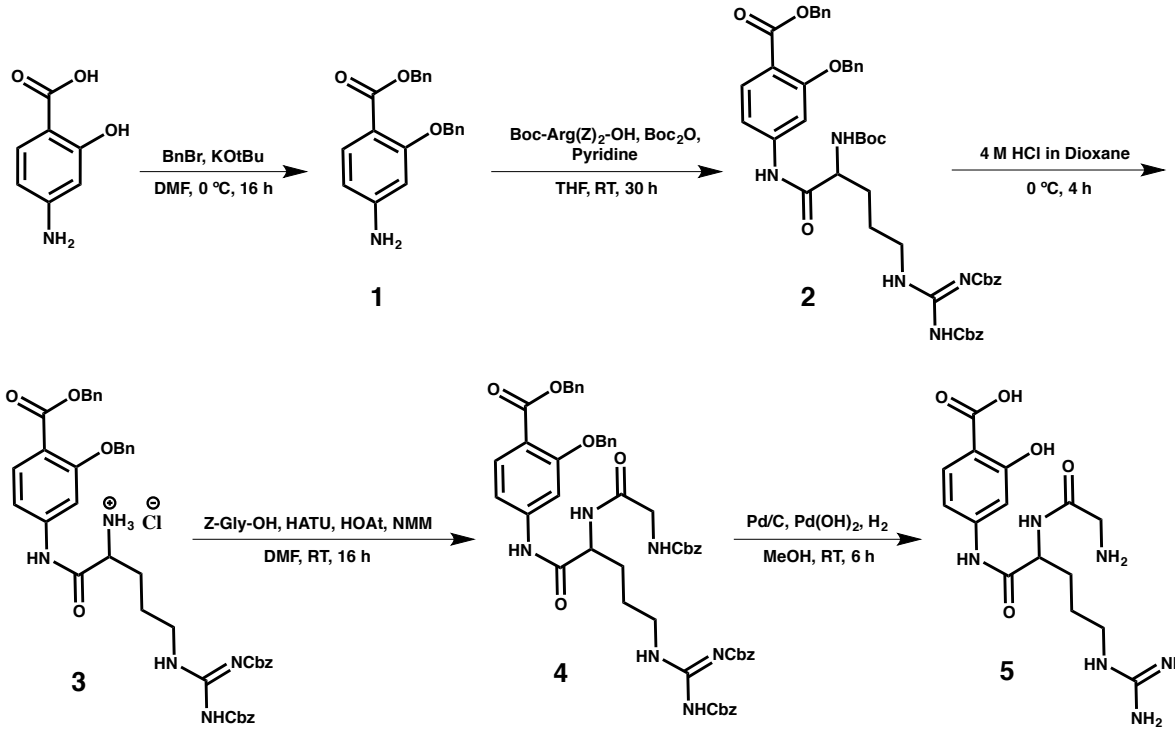

Scheme 2.1. *Synthetic scheme for the catalyCEST MRI contrast agent,* ***5****.*

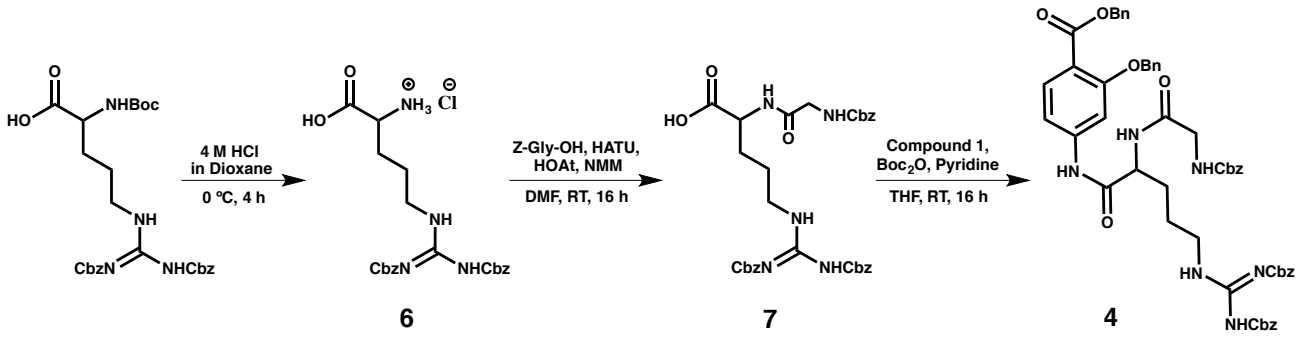

Scheme 2.2. *Alternative scheme for synthesis of the precursor,* ***4****, to the catalyCEST MRI contrast agent.*

Synthesis of Compound 1

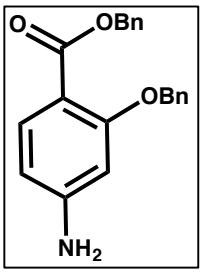

Compound **1** was synthesized from a reported procedure (**Scheme 2.1**).[18] To a stirred solution of 4-aminosalicylic acid (19.7 mmol, 3.0 g) in dry dimethyl formamide in a 500 mL round bottom flask, KO*t*Bu (21.5 mmol, 1.1 equiv, 2.4 g) was added all at once. After the reaction mixture was cooled to 0 °C, benzyl bromide (21.6 mmol, 1.1 equiv, 2.6 mL) was added drop-wise. The reaction mixture was allowed to warm to room temperature and stir for 5 h. Then, a second portion of KO*t*Bu (21.5 mmol, 1.1 equiv, 2.4 g) was added. After the reaction mixture was cooled to 0 °C, benzyl bromide (21.6 mmol, 1.1 equiv, 2.6 mL) was added drop-wise. The reaction mixture was allowed to warm to room temperature and stir for 16 h before quenching with H_2O. The solution was extracted with ethyl acetate. The organic layer was washed with brine then concentrated, dried over Na_2SO_4, filtered, and the solvent was removed by rotary evaporation. The crude mixture was purified by flash column chromatography over SiO_2 (3:7 ethyl acetate:hexanes) to yield compound **1** as a white powder (7.4 mmol, 2.5 g, 38%). ^{1}H NMR (400 MHz, $CDCl_3$) δ 7.81 (d, J = 9.0 Hz, 1H), 7.48-7.44 (m, 2H), 7.41-7.27 (m, 8H), 6.26-6.23 (m, 2H), 5.31 (s, 2H), 5.13 (s, 2H), 4.01 (br. s, 2H). LRMS-ESI (m/z): $[M+H]^+$ calculated for $[C_{21}H_{20}NO_3]$, 334.1; found, 334.2

Synthesis of Compound 2

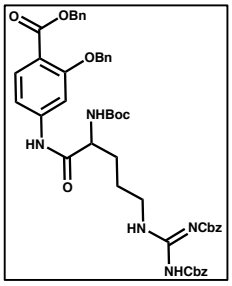

Compound **2** was synthesized from a reported procedure with slight modifications (**Scheme 2.1**).[19] Boc-Arg(Z)$_2$-OH (7.8 mmol, 1.1 equiv, 4.2 g) was dissolved in 70 mL tetrahydrofuran and treated dropwise with anhydrous pyridine (7.8 mmol, 1.1 equiv, 0.63 mL) in a 300 mL round-bottom flask. To this solution, 2M Boc-anhydride in tetrahydrofuran (7.8

mmol, 1.1 equiv, 3.9 mL) was added, and the mixture was allowed to stir at room temperature for 1 h. Then, a solution of compound **1** (7.1 mmol, 2.4 g) in 15 mL tetrahydrofuran was added to the flask and the reaction mixture was allowed to stir at room temperature for 30 h. On completion, the reaction mixture was diluted with ethyl acetate and washed with saturated $NaHCO_3$, followed by 1 M HCl, and water. The organic layer was washed with brine then concentrated, dried over Na_2SO_4, filtered, and the solvent was removed by rotary evaporation. The crude mixture was purified by flash column chromatography over SiO_2 (3:7 ethyl acetate:hexanes) to yield compound **2** as a yellow oil (5.5 mmol, 4.7 g, 77%). ^{1}H NMR (600 MHz, $CDCl_3$) δ 9.40 (br. s, 1H), 9.26 (br. s, 1H), 8.66 (s, 1H), 7.66 (d, J = 8.5 Hz, 1H), 7.50 (s, 1H), 7.38-7.35 (m, 2H), 7.33-7.12 (m, 18H), 6.44 (d, J = 8.1 Hz, 1H), 5.79 (s, 1H), 5.24 (s, 2H), 5.16 (s, 2H), 5.11-4.95 (m, 4H), 4.36 (s, 1H), 4.04-3.77 (m, 2H), 1.82-1.54 (m, 4H), 1.37 (s, 9H). LRMS-ESI (m/z): $[M+H]^+$ calculated for $[C_{48}H_{52}N_5O_{10}]$, 858.4; found, 858.4

Synthesis of Compound 3

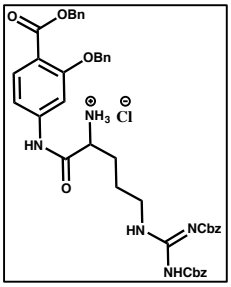

Compound **3** was synthesized from a reported procedure with slight modifications (**Scheme 2.1**).[20] To a 100 mL round-bottom flask with compound **2** (4.2 mmol, 3.6 g), 4 M HCl in dioxane (44 mL) was added cold and stirred for 4 h until TLC showed that no starting material remained (1:1 ethyl acetate:hexanes). After the solvent was removed by rotary evaporation, the product was purified by preparative HPLC (RP C-18, 10-90 0.1% TFA:acetonitrile in 45 min, R_t = 29.39 min) and lyophilized to yield compound **3** as a white solid (1.8 mmol, 1.4 g, 42%). ^{1}H NMR (400 MHz, $CDCl_3$) δ 10.52 (s, 1H), 9.61 (br. s, 1H),

7.71 (d, *J* = 8.5 Hz), 7.43-7.17 (m, 21H), 7.09 (dd, *J* = 8.5, 1.6 Hz, 1H), 5.26 (s, 2H), 5.22-5.02 (m, 4H), 4.98 (s, 2H), 4.55-4.47 (m, 1H), 3.82-3.66 (m, 2H), 2.11-1.75 (m, 4H).

Synthesis of Compound 4

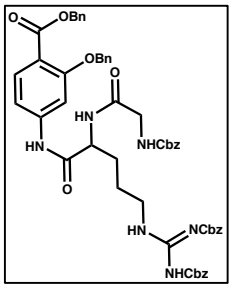

Compound **4** was synthesized (**Scheme 2.1**) by dissolving Z-Gly-OH (1.9 mmol, 1.1 equiv, 0.41 g), 2-(7-Aza-1H-benzotriazole-1-yl)-1,1,3,3-tetramethyluronium hexafluoro-phosphate, (HATU, 2.1 mmol, 1.2 equiv, 0.81 g) and 1-hydroxy-7-azabenzotriazole, (HOAt, 2.1 mmol, 1.2 equiv, 0.29 g) in 80 mL of dimethyl formamide in a 250 mL round-bottom flask. After the reaction mixture was cooled to 0 °C, N-methyl morpholine (3.5 mmol, 2.0 equiv, 0.39 mL) was added drop-wise and allowed to equilibrate for 15 min. Compound **3** (1.8 mmol, 1.4 g) was dissolved in 15 mL of dimethyl formamide and then added to the flask. The ice bath was removed, and the reaction mixture was allowed to stir at room temperature overnight. The reaction mixture was diluted with ethyl acetate and washed with 5% $NaHCO_3$, 5% citric acid, and water. The organic layer was washed with brine then concentrated, dried over Na_2SO_4, filtered, and the solvent was removed by rotary evaporation. The product was purified by preparative HPLC (RP C-18, 10-90 0.1% TFA:acetonitrile in 45 min, R_t = 40.97 min). The solvent was removed by rotary evaporation to yield compound **4** as a yellow oil (0.90 mmol, 0.86 g, 51%). ^{1}H NMR (400 MHz, $CDCl_3$) δ 9.66 (br. s, 1H), 9.40 (s, 1H), 8.49 (br. s, 1H), 8.05 (d, *J* = 7.0 Hz, 1H), 7.81 (d, *J* = 8.5 Hz, 1H), 7.67 (s, 1H), 7.48-7.43 (m, 2H), 7.41-7.18 (m, 23H), 7.05 (d, *J* = 8.3 Hz, 1H), 5.71 (s, 1H), 5.32 (s, 2H), 5.27 (d, *J* = 4.1 Hz, 2H), 5.12 (s, 2H), 5.11-5.08 (m, 2H), 5.06 (d, *J* =7.7 Hz, 2H), 4.67 (m, 1H), 4.06-3.56 (m, 4H), 1.95-1.57 (m, 4H). LRMS-ESI (m/z): $[M+H]^+$ calculated for $[C_{53}H_{53}N_6O_{11}]$, 949.37; found, 949.43

Attempted Synthesis of Compound 4

An alternative synthesis of compound **4** was attempted using a reported procedure with slight modifications (**Scheme 2.2**).[19] Compound **7** (4.2 mmol, 2.6g) was dissolved in 40 mL tetrahydrofuran and treated dropwise with anhydrous pyridine (4.2 mmol, 0.34 mL) in a 250 mL round-bottom flask. To this solution, 2M Boc-anhydride in tetrahydrofuran (4.2 mmol, 2.1 mL) was added, and the mixture was allowed to stir at room temperature for 1 h. Then, a solution of compound **1** (4.6 mmol, 1.1 equiv, 1.5 g) in 8 mL tetrahydrofuran was added to the flask and the reaction mixture was allowed to stir at room temperature for 16 h. On completion, the reaction mixture was diluted with ethyl acetate and washed with saturated $NaHCO_3$, followed by 1 M HCl, and water. The organic layer was washed with brine then concentrated, dried over Na_2SO_4, and the solvent was removed by rotary evaporation. The crude mixture was purified by flash column chromatography over SiO_2 (3:7 ethyl acetate:hexanes). Multiple spots were collected, but none of the spots were identified as compound **4**.

Synthesis of Compound 5

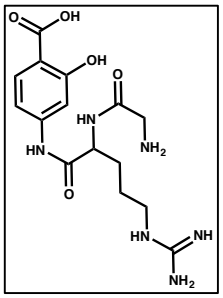

To synthesize compound **5** (**Scheme 2.1**), compound **4** (0.56 mmol, 0.54 g) was dissolved in 48 mL methanol in a 250 mL round-bottom flask, and 0.4 mL of 1 M HCl in 16 mL ethyl acetate was added to the solution for solubility. A catalytic amount of Pd/C (15% w/w) and $Pd(OH)_2$ (15% w/w) were added to the reaction mixture. The round-bottom flask was then equipped with a H_2 balloon and stirred for 6 h. The reaction mixture was passed over a medium frit filter with celite, and then, the solvent was removed by rotary evaporation. The compound was purified over a Sep Pak column (1:1 water with 0.1% trifluoroacetic

acid:acetonitrile). The final compound was purified by preparative HPLC (RP C-18, 0-30 0.1%TFA:acetonitrile in 45 min, R_t = 13.06 min) and lyophilized to yield compound **5** as a white solid (0.53 mmol, 0.20 g, 96%). ^{1}H NMR (499 MHz, D_2O) δ 7.83 (d, *J* = 8.7 Hz, 1H), 7.18 (d, *J* = 2.0 Hz), 7.00 (dd, *J* = 8.7, 2.1 Hz, 1H), 4.48 (dd, *J* = 7.8, 6.1 Hz, 1H), 3.90 (s, 2H), 3.21 (t, *J* = 6.9 Hz, 2H), 1.98-1.81 (m, 2H), 1.77-1.61 (m, 2H). ^{13}C NMR (125 MHz, D_2O) δ 172.1, 171.8, 167.1, 160.8, 156.7, 143.3, 140.0, 131.8, 112.3, 108.1, 54.4, 40.5, 40.3, 28.3, 24.4. HRMS-ESI (m/z): $[M+H]^+$ calculated for $[C_{15}H_{23}N_6O_5]$, 367.1724; found, 367.1729

Synthesis of Compound 6

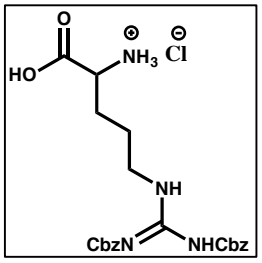

Compound **6** was synthesized from a reported procedure with slight modifications (**Scheme 2.2**).[20] To a 100 mL round-bottom flask with Boc-Arg$(Z)_2$-OH (0.47 mmol, 0.26 g), 4 M HCl in dioxane (3.1 mL) was added cold and stirred for 4 h until TLC showed that no starting material remained (1:1 ethyl acetate:hexanes). After the solvent was removed by rotary evaporation, the product was purified by preparative HPLC (RP C-18, 10-90 0.1% TFA:acetonitrile in 45 min, R_t = 16.12 min) and lyophilized to yield compound **6** as a white solid (0.46 mmol, 0.22 g, 98%). ^{1}H NMR (400 MHz, $CDCl_3$) δ 8.07 (br. s, 2H), 7.40 – 7.25 (m, 10H), 6.93 (br. s, 1H), 5.33 (d, *J* = 2.4 Hz, 2H), 5.25 (s, 2H), 5.06 – 5.24 (m, 2H), 4.05 (s, 1H), 3.87 – 3.96 (m, 2H), 1.67 – 2.09 (m, 4H).

Attempted Synthesis of Compound 6

The synthesis of compound **6** was attempted using a reported procedure.[21] To a 100 mL round-bottom flask with Boc-Arg$(Z)_2$-OH (0.93 mmol, 0.50 g) in dry dichloromethane (4.6 mL), $AlCl_3$ (0.93 mmol, 0.13 g) was added at 0 °C. The ice bath was removed, and the reaction mixture was allowed to stir at room temperature for 2 h. The reaction mixture was

diluted with ethyl acetate and washed with aqueous $NaHCO_3$. The organic layer was washed with brine then concentrated, dried over Na_2SO_4, filtered, and the solvent was removed by rotary evaporation to yield starting material.

Synthesis of Compound 7

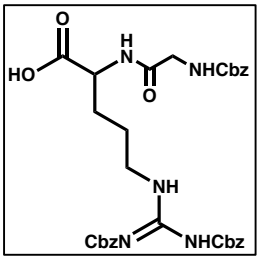

Compound **7** was synthesized (**Scheme 2.2**) by dissolving Z-Gly-OH (0.51 mmol, 1.1 equiv, 0.11 g), 2-(7-Aza-1H-benzotriazole-1-yl)-1,1,3,3-tetramethyluronium hexafluoro-phosphate, (HATU, 0.55 mmol, 1.2 equiv, 0.21 g) and 1-hydroxy-7-azabenzotriazole, (HOAt, 0.55 mmol, 1.2 equiv, 0.08 g) in 24 mL of dimethyl formamide in a 100 mL round-bottom flask. After the reaction mixture was cooled to 0 °C, N-methyl morpholine (0.92 mmol, 2.0 equiv, 0.10 mL) was added drop-wise and allowed to equilibrate for 15 min. Compound **6** (0.46 mmol, 0.22 g) was dissolved in 8 mL of dimethyl formamide and then added to the flask. The ice bath was removed, and the reaction mixture was allowed to stir at room temperature overnight. The reaction mixture was diluted with ethyl acetate and washed with 5% $NaHCO_3$, 5% citric acid, and water. The organic layer was washed with brine then concentrated, dried over Na_2SO_4, filtered, and the solvent was removed by rotary evaporation. The product was purified by preparative HPLC (RP C-18, 10-90 0.1% TFA:acetonitrile in 45 min, R_t = 27.45 min). The solvent was removed by rotary evaporation to yield compound 4 as a white solid (0.04 mmol, 0.02 g, 8%). ^{1}H NMR (400 MHz, $CDCl_3$) δ 9.85 (s, 1H), 7.86 (d, J = 7.5 Hz, 1H), 7.45 – 7.13 (m, 15H), 5.32 (s, 2H), 5.23 (s, 2H), 5.02 (s, 2H), 4.46 (s, 1H), 3.99-3.76 (m, 2H), 3.83 (s, 2H), 1.93 – 1.61 (m, 4H).

2.2.2. *In Vivo* CatalyCEST MRI Studies

All *in vivo* studies were approved by the Institutional Animal Care and Use Committee of the University of Arizona. To prepare the mouse models of pancreatic cancer, SCID female mice that were 6 weeks old were injected subcutaneously with 1×10^6 Capan-2 tumor cells suspended in 200 μL of saline and Matrigel in the right flank. All imaging studies were performed 28-37 days post injection when the tumor reached approximately 400 mm^3 in volume.

MRI studies were performed with a preclinical Bruker MRI scanner (Bruker Biospin, Inc., Billerica, MA) operating at 7.05 T (300 MHz) magnetic field strength with a 72 mm quadrature transceiver coil. To detect *in vivo* uPA enzyme activity, catalyCEST MRI studies were performed with 10 mice bearing Capan-2 tumors. Each mouse was anesthetized with 1.0-2.0% isoflurane delivered in 1 L/min oxygen gas ventilation. The mouse was then secured to a customized MRI–compatible cradle, probes for monitoring rectal temperature and respiration were connected to the mouse, and core body temperature was regulated at 37.0 ± 0.2 °C using an air heater (SA Instruments, Inc., Stony Brook, NY). Once the mouse was secured, the agent solution of 250 mM in 200 μL of 1x sterile PBS was injected into the mouse subcutaneously near the tumor. An initial set of images were acquired to help locate the tumor, using a multi-slice-multi-echo MRI protocol with the following parameters, TR: 2000 ms; TE: 10.00 ms; excitation flip angle: 90°; axial image orientation matrix: 192×192; field of view: 4.8x4.8 cm; in-plane spatial resolution: 250x250 μm; slice thickness: 2 mm; number of slices: 1; number of averages: 1; total scan time: 6:24 min. Once the agent had 10 min to incubate to allow for enzyme cleavage, the *in vivo* CEST-FISP MRI studies were carried out with the following parameters, TR: 4.390 ms; TE: 1.995 ms; excitation flip

angle: 15°; with radiofrequency spoiling; centric encoding during acquisition; matrix: 96×96; field of view: 4.8x4.8 cm; in-plane spatial resolution: 500x500 μm; slice thickness: 2 mm; number of slices: 1; number of averages: 1; total scan time: 5:34 min. A continuous 5 s wave pulse at a saturation power of 4 μT was used at each saturation frequency. Each catalyCEST MRI scan was acquired with a series of 46 saturation frequencies at ppm values of +16, +15, +14, +13.8 to 3.0 (with 0.4 ppm increments), +2.5 to -2.0 (with 0.5 ppm increments), and -3 to -12 (with 2 ppm increments). Twelve consecutive CEST spectra were collected. At the end of the MR scan, the mouse was allowed to recover after being removed from the magnet and cradle.

To obtain parametric maps of the CEST signal amplitudes during *in vivo* catalyCEST MRI studies, the images from the last six repetitions were averaged, and a Gaussian spatial filter was applied to the average image with a 3×3 pixel matrix and a σ value of one ixel.[22] The region of interest (ROI) for the location of the agent was determined from the CEST MR images. The CEST spectrum from each pixel in the image was obtained from the MR images. Linear baseline correction was applied to account for power drift of the gradient amplifier, and possible heating of the static shim coils or sample. A function of four Lorentzian line shapes was fit to each CEST spectrum to measure the signal amplitudes of the CEST effects at 5.0 and 9.5 ppm, and also account for direct saturation of water and the endogenous effect of amide proton transfer.[23] The saturation frequency, width, and amplitude of the Lorentzian line shape that fit the direct saturation of water was allowed to change during the fitting procedure. The width and amplitude of the two Lorentzian line shapes that fit the CEST effects of the agent were also allowed to change, but the saturation frequencies of these Lorentzian line shapes were fixed at 9.5 and 5.0 ppm relative to the saturation

frequency of the direct saturation of water. The parametric maps of the reaction coordinate of uPA enzyme activity were determined using **Eq. [1]**. The resulting images were evaluated in ImageJ, and average values of brightness were obtained.

$$\text{Reaction Coordinate} = 1 - \frac{CEST\ signal\ amplitude\ at\ 5.0\ ppm}{CEST\ signal\ amplitude\ at\ 9.5\ ppm} \qquad \text{Eq. [1]}$$

2.2.3. *In Vivo* CatalyCEST MRI Studies with BTZ

The effect of BTZ on uPA activity was studied with *in vivo* catalyCEST MRI. A set of 4 mice were injected IV with a dose of 2 mg/kg in 150 μL of 10% dimethyl sulfoxide and 90% sterile saline. CatalyCEST MRI studies were performed 3 h after injection using the same CEST–FISP MRI protocol as used for the *in vivo* detection of enzyme activity. Control studies were also performed with a set of 3 mice. Sterile saline (150 μL) was injected IV into the mouse, and catalyCEST MRI studies were performed 3 h later using the same CEST-FISP MRI protocol. An additional 3 mice were scanned with catalyCEST MRI and were then euthanized without treatment, to provide pre-treatment samples for *ex vivo* studies. Analysis of *in vivo* CEST MRI and parametric maps were generated in a same way as described earlier for *in vivo* enzyme activity analysis.

2.2.4. *Ex Vivo* Studies

The total uPA activity was analyzed using a commercially available uPA Activity Assay Kit (ECM600 Kit, Millipore, Inc., Billerica, MA). A linear calibration curve was constructed per the manufacturer's instructions by preparation of a chromogenic substrate and human urine uPA provided with the kit. A Synergy 2 microplate reader (Biotek Instruments Inc., Winooski, VA) was used to monitor absorbance at 405 nm. The amount of uPA activity varied between 0.37 and 1.20 Units for the standard curve.

To determine *in vivo* uPA activity, Capan-2 tumors were harvested from mice after euthanasia with cervical dislocation immediately after the scan. The tumor samples were placed into cryovials and frozen in liquid nitrogen. The samples were stored at -80 °C until they were analyzed at one time with the uPA Activity Assay Kit. About 200 mg of sample was placed in 500 μL of 1× assay buffer from the uPA Activity Assay Kit. Samples were homogenized with a handheld Powergen homogenizer (Fisher Scientific, Waltham, MA) and sonicated. The samples were centrifuged at 2000*g* for 5 min at room temperature. The supernatant was transferred to a new tube and the pellet discarded. This step was repeated 3× for a total spin of 15 min. The uPA activity of the experimental samples was measured after 1.5 h of incubation with the substrate. The amount of uPA activity in each experimental sample was determined from the calibration curve and normalized to total protein per well. The total protein content was measured using a 660 nm Protein Assay kit (Thermo Scientific, Rockford, IL).

2.3. Results

2.3.1. Synthesis of Contrast Agent

The contrast agent, compound **5,** was synthesized with an overall yield of 6%, which followed a 5-step synthesis strategy (**Scheme 2.1**). First, the acid functional group of 4-amino salicylic acid was protected as a benzyl ester followed by protection of the hydroxyl functional group as a benzyl alcohol. Then, the arginine amino acid was coupled to the amino group by standard peptide coupling procedures. After deprotection of the Boc group on the arginine, the glycine amino acid was coupled by standard peptide coupling

procedures. The final deprotection step by hydrogenation produced the contrast agent, which was purified and used for the catalyCEST studies.

2.3.2. *In Vivo* CatalyCEST MRI Studies

The catalyCEST MRI study detected two signals from the contrast agent at 9.5 and 5.0 ppm (relative to the water resonance defined to be 0 ppm for MRI studies). These CEST signals were assigned to the salicylic acid proton and the aryl amide proton, respectively.

The mice were first imaged 48 h before treatment to establish baseline uPA activity. Of the 10 mice, 3 were sacrificed immediately after the baseline scan (**Figure 2.3**) for *ex vivo* analysis. Of the remaining 7, 4 mice were treated with BTZ and scanned again after 3 h **(Figure 2.4a,b,c**). The other 3 mice were treated with sterile saline and scanned after 3 h (**Figure 2.4d,e,f**). All the treated mice were sacrificed immediately after the scan for *ex vivo* analysis.

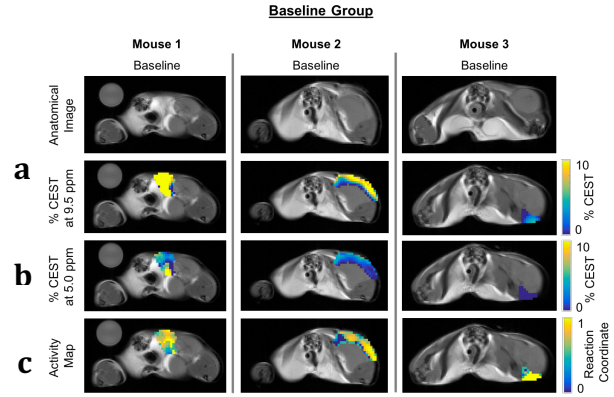

Figure 2.3. In vivo *catalyCEST MR images of baseline mice. (a) Anatomical images of the three mice that were sacrificed after the baseline scan. (b) Parametric maps of % CEST signal amplitudes of CEST at 9.5 and 5.0 ppm observe presence of contrast agent in the areas around the tumors. (c) Activity maps of uPA enzyme show high activity near the outside of the tumor.*

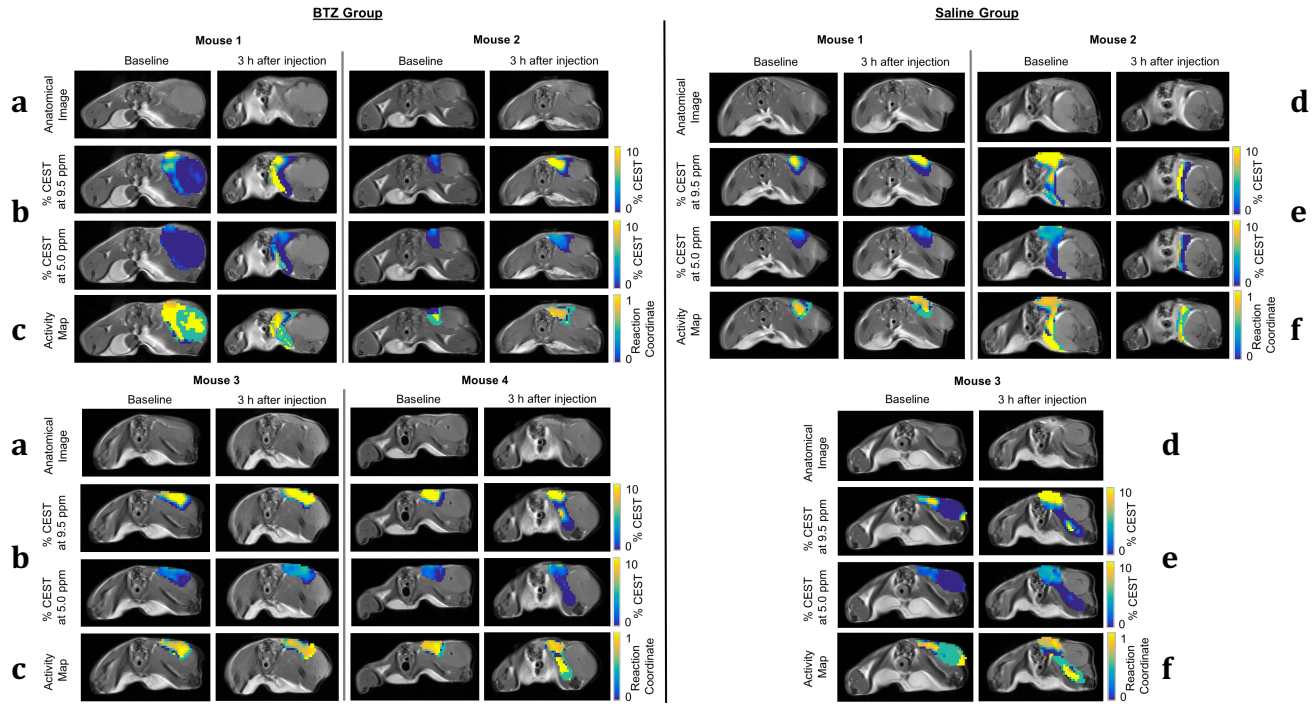

Figure 2.4. In vivo *catalyCEST MR images of mice before and after treatment with BTZ or saline. Each mouse was imaged at baseline and then at 3 h post-injection. (a, d) Anatomical images of the four mice that were injected with BTZ (a) and with saline (d). (b, e) Parametric maps of % CEST signal amplitudes of CEST at 9.5 and 5.0 ppm observe presence of contrast agent in the areas around the tumors for mice injected with BTZ (b) and with saline (e). (c, f) Activity maps of uPA enzyme show high activity near the outside of the tumor for mice injected with BTZ (c) and with saline (f).*

From the activity maps, the mean reaction coordinate for each of the images was obtained, and the average of each group was taken (**Figure 2.5**). The average of the mean

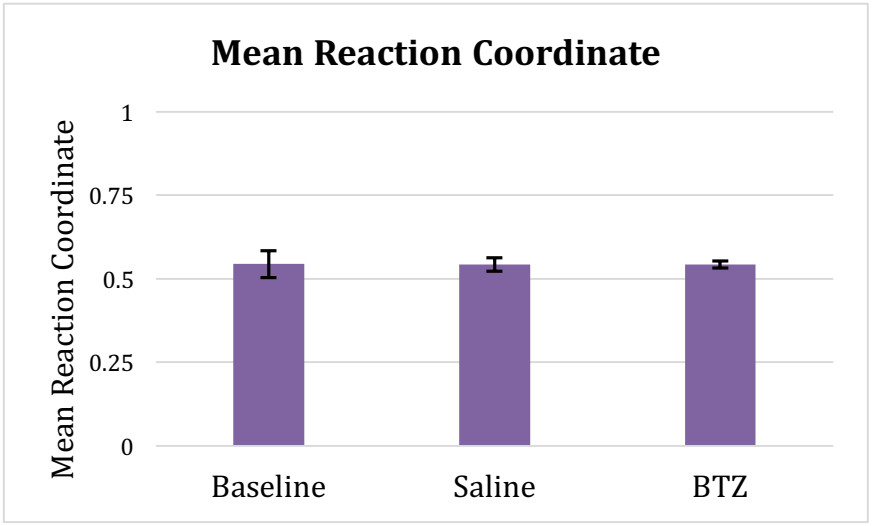

Figure 2.5. *Chart of mean reaction coordinates for baseline, saline, and BTZ groups. The bar graph on the left indicates the average value of the mean reaction coordinate for the baseline scans of the 10 mice. The bar in the middle indicates the average value of the mean reaction coordinate for the 3 scans acquired 3 h post saline injection. The bar on the right indicates the average value of the mean reaction coordinate for the 4 scans acquired 3 h post BTZ injection. The standard deviation is shown for each bar.*

reaction coordinate for the 10 baseline scans was 0.54 ± 0.04. The average of the mean reaction coordinate for the 3 post saline injection scans was 0.54 ± 0.02. The average of the mean reaction coordinate for the 4 post BTZ injection scans was 0.54 ± 0.01. A p-value was calculated for each combination of groups: baseline vs. saline ($p = 0.94$), baseline vs. BTZ ($p = 0.95$), and saline vs. BTZ ($p = 0.97$). Also, the mean reaction coordinate for each scan was plotted against the tumor volume to look for correlations (**Figure 2.6**). The R^2 value for the calculated trendline was 0.034.

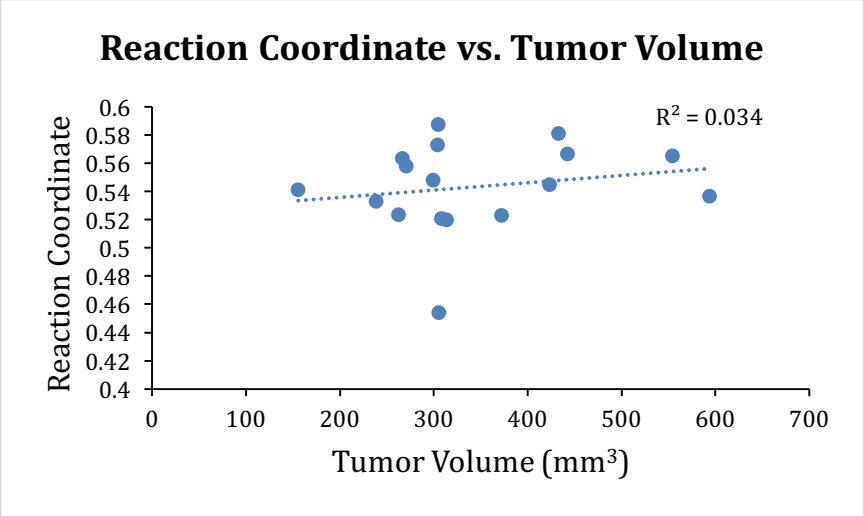

Figure 2.6. *Chart of reaction coordinate vs. the tumor volume. The reaction coordinates of all the 17 scans are paired with the corresponding tumor volumes.*

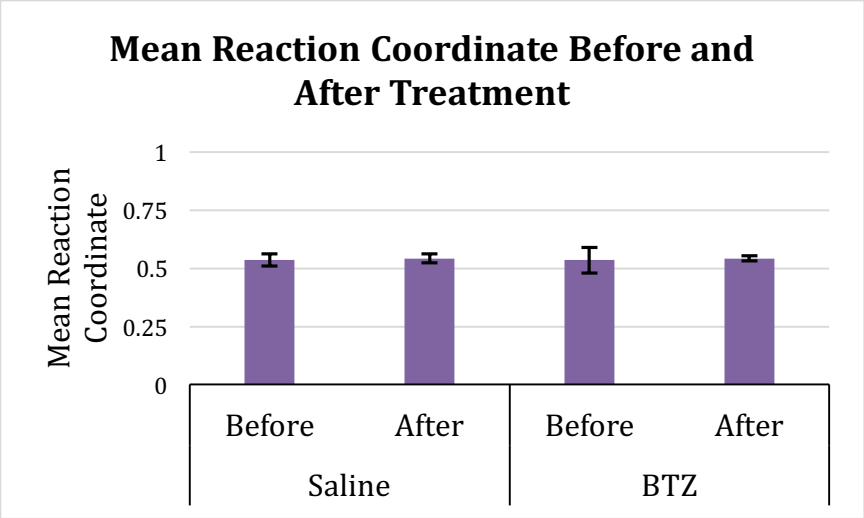

Figure 2.7. *Chart of mean reaction coordinates for before and after treatment groups of saline and BTZ. The two bars on the right indicate the average value of the mean reaction coordinate for the 3 mice in the saline group. The two bars on the left indicated the average value of the mean reaction coordinate for the 4 mice in the BTZ group. The standard deviation is shown for each bar.*

Additionally, the average of the mean reaction coordinates before and after treatment was calculated from the activity maps (**Figure 2.7**). The average of the mean reaction coordinates before and after the saline injection were 0.54 ± 0.03 and 0.54 ± 0.02 ($p = 0.49$), respectively. The average of the mean reaction coordinates before and after the BTZ injection were 0.54 ± 0.06 and 0.54 ± 0.01 ($p = 0.46$), respectively.

2.3.3. *Ex Vivo* Studies

The uPA activity *ex vivo* was determined from the frozen tumors (**Figure 2.8**). The average baseline activity was 0.86 ± 0.10 relative units. The average activity after saline

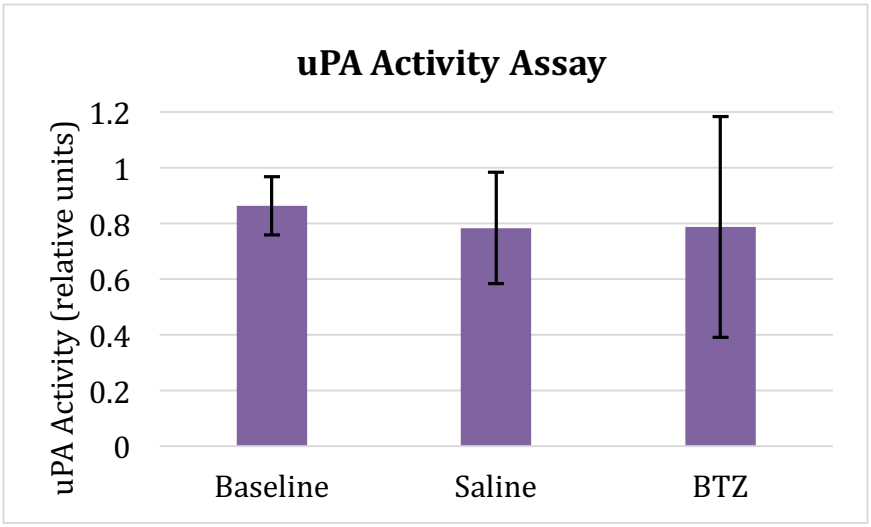

Figure 2.8. Ex vivo *uPA enzyme activity. The average uPA activity for the baseline (3 samples), saline-treated (3 samples), and BTZ-treated tumors (4 samples).*

treatment was 0.78 ± 0.20 relative units. Lastly, the average activity after BTZ treatment was 0.79 ± 0.40 relative units.

The uPA activity in relative units was plotted against the tumor volumes at the time of the final scan (**Figure 2.9**). The R^2 value of the calculated trendline was 0.0044. Lastly, uPA activity was plotted against the reaction coordinates of the corresponding images (**Figure 2.10**). The R^2 value for the calculated trendline was 0.068.

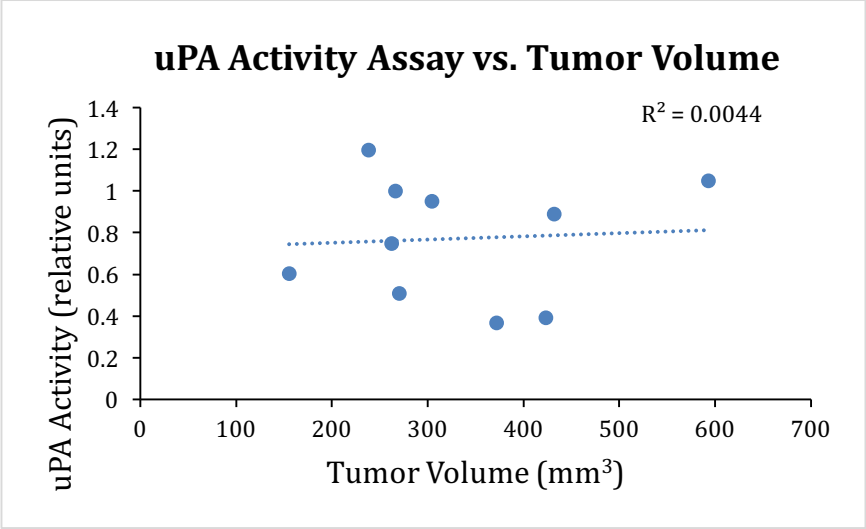

Figure 2.9. *Chart of uPA activity of the frozen tumors vs. tumor volume before the final scan for each mouse.*

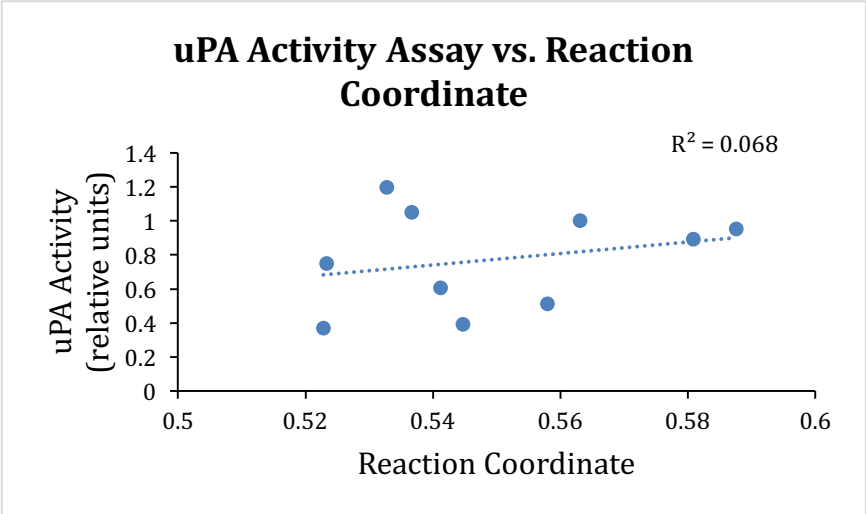

Figure 2.10. *Chart of uPA activity of the frozen tumors vs. the final scan for each mouse.*

2.4. Discussion

2.4.1. Synthesis of Contrast Agent

The previously reported synthetic route for this contrast agent was optimized over the course of this project.[24] Originally, compound **2** was deprotected using concentrated HCl. This procedure deprotected the Boc group and also combinations of the Cbz and Bn groups. The standard procedure for Boc deprotection is TFA; however, using TFA resulted in the same problem of deprotecting multiple groups. Finally, 4 M HCl in dioxane allowed for the deprotection of Boc with minor deprotection of other groups. Also, HPLC purification was required for this step due to the polarity of the ammonium salt. The synthesis of compound **4** originally used benzotriazol-1-yloxy tris(dimethylamino)phosphonium hexafluorophosphate (BOP) and hydroxybenzotriazole (HOBt) as the coupling reagents.[24] However, in order to increase yield, BOP and HOBt were replaced with HATU and HOAt, more robust reagents. Additionally, flash column chromatography was unsuccessful in separating the compound from the byproducts, which were very similar in polarity, so HPLC was used for purification of compound **4**.

The pure contrast agent is a white solid and is very soluble in water. When dissolved in 1x PBS, the contrast agent makes the solution extremely acidic of about 0.3 pH. When the pH is adjusted to a more neutral pH, the clear solution turns yellow. The color change is likely due to the deprotonation of a group on the salicylic acid ring.

2.4.2. *In Vivo* CatalyCEST MRI Studies

Previous preliminary work indicated that a decrease in uPA activity could be observed 3 h after chemotherapy was administered (data not published). However, the results from this study show that no change in activity was observed.

The parametric activity maps (**Figure 2.3** and **Figure 2.4**) showed no contrast agent uptake in the tumor. Rather most of the activity was observed in the area around the tumor where the contrast agent was injected subcutaneously. Tumor uptake could have been influenced by the formulation of the contrast agent. Additionally, injecting the agent subcutaneously may have led to poor uptake due to the biology of the tumor. In the future, injecting the contrast agent IV should be considered to improve the uptake in the tumor and move to a more clinically applicable approach. The averages of the mean reaction coordinates for extracellular uPA activity for the baseline, saline, and BTZ groups (**Figure 2.5**) were statistically the same (baseline vs. BTZ, $p > 0.05$; saline vs. BTZ, $p > 0.05$; baseline vs. saline, $p > 0.05$). Additionally, there was no statistical difference before and after treatment of BTZ ($p > 0.05$) (**Figure 2.7**). No correlation was found between the mean reaction coordinates and the tumor volumes (**Figure 2.6**) with an R^2 value of 0.034. Based on these results, it is difficult to determine the sensitivity of the contrast agent and the CEST technique for uPA activity in the *in vivo* data. Other proteases may have cleaved the peptide sequence and made it seem as though uPA activity was high. More *in vivo* testing with different controls would have to be done in order to have a definitive answer.

2.4.3. *Ex Vivo* Studies

The *ex vivo* analysis provided similar results. The relative intracellular uPA activity of the baseline, saline, and BTZ groups (**Figure 2.8**) were also statistically the same

(baseline vs. BTZ, $p > 0.05$; saline vs. BTZ, $p > 0.05$; baseline vs. saline, $p > 0.05$). There was no correlation found between uPA activity and tumor volume ($R^2 = 0.004$) (**Figure 2.9**). Lastly, no correlation was found between mean reaction coordinate and uPA activity (**Figure 2.10**) with an R^2 value of 0.068. The *in vivo* and the *ex vivo* results may be difficult to correlate because extracellular uPA activity *in vivo* is being compared to intracellular activity *ex vivo*. The results for the *ex vivo* data may have been inconclusive due to the instability of uPA. Even though precautions were taken to preserve the enzyme (e.g., excising and freezing the tumors immediately after the scan), the samples were analyzed 1-2 weeks after they were frozen, which may have led uPA to degrade. One way of addressing this issue is to run assays immediately after the scan with fresh samples. Another way to overcome the instability of uPA is to analyze the activity of an enzyme upstream (e.g., NF-κB) of uPA in the cascade. From the current results, no meaningful conclusions could be drawn about the effect of BTZ on uPA activity.

2.5. References for Chapter 2

1. McKay, L. I.; Cidlowski, J. A., Molecular control of immune/inflammatory responses: interactions between nuclear factor-κB and steroid receptor-signaling pathways. *Endocrine Reviews* **1999,** *20* (4), 435-459.

2. Andela, V. B.; Schwarz, E. M.; Puzas, J. E.; O'Keefe, R. J.; Rosier, R. N., Tumor metastasis and the reciprocal regulation of prometastatic and antimetastatic factors by nuclear factor κB. *Cancer Research* **2000,** *60* (23), 6557-6562.

3. Crippa, M. P., Urokinase-type plasminogen activator. *The International Journal of Biochemistry & Cell Biology* **2007,** *39* (4), 690-694.

4. Das, R.; Philip, S.; Mahabeleshwar, G. H.; Bulbule, A.; Kundu, G. C., Osteopontin: it's role in regulation of cell motility and nuclear factor κB-mediated urokinase type plasminogen activator expression. *IUBMB Life* **2005,** *57* (6), 441-447.

5. Mekkawy, A. H.; Pourgholami, M. H.; Morris, D. L., Involvement of urokinase-type plasminogen activator system in cancer: an overview. *Medicinal Research Reviews* **2014,** *34* (5), 918-956.

6. Andreasen, P. A.; Kjøller, L.; Christensen, L.; Duffy, M. J., The urokinase-type plasminogen activator system in cancer metastasis: a review. *International Journal of Cancer* **1997,** *72* (1), 1-22.

7. Wang, Y., The role and regulation of urokinase-type plasminogen activator receptor gene expression in cancer invasion and metastasis. *Medicinal Research Reviews* **2001,** *21* (2), 146-170.

8. Duffy, M. J.; O'Siorain, L.; O'Grady, P.; Devaney, D.; Fennelly, J. J.; Lijnen, H. J., Urokinase‐plasminogen activator, a marker for aggressive breast carcinomas. Preliminary report. *Cancer* **1988,** *62* (3), 531-533.

9. Oka, T.; Ishida, T.; Nishino, T.; Sugimachi, K., Immunohistochemical evidence of urokinase-type plasminogen activator in primary and metastatic tumors of pulmonary adenocarcinoma. *Cancer Research* **1991,** *51* (13), 3522-3525.

10. Hasui, Y.; Marutsuka, K.; Suzumiya, J.; Kitada, S.; Osada, Y.; Sumiyoshi, A., The content of urokinase‐type plasminogen activator antigen as a prognostic factor in urinary bladder cancer. *International Journal of Cancer* **1992,** *50* (6), 871-873.

11. Nekarda, H.; Siewert, J.; Schmitt, M.; Ulm, K., Tumour-associated proteolytic factors uPA and PAI-1 and survival in totally resected gastric cancer. *The Lancet* **1994,** *343* (8889), 117.

12. Mulcahy, H.; O'Donoghue, D.; Duffy, M.; Gibbons, D.; McCarthy, P.; Parfrey, N.; Sheahan, K., Urokinase-type plasminogen activator and outcome in Dukes' B colorectal cancer. *The Lancet* **1994,** *344* (8922), 583-584.

13. Kobayashi, H.; Fujishiro, S.; Terao, T., Impact of urokinase-type plasminogen activator and its inhibitor type 1 on prognosis in cervical cancer of the uterus. *Cancer Research* **1994,** *54* (24), 6539-6548.

14. Kuhn, W.; Pache, L.; Schmalfeldt, B.; Dettmar, P.; Schmitt, M.; Jänicke, F.; Graeff, H., Urokinase (uPA) and PAI-1 predict survival in advanced ovarian cancer patients (FIGO III) after radical surgery and platinum-based chemotherapy. *Gynecologic Oncology* **1994,** *55* (3), 401-409.

15. Hofmann, R.; Lehmer, A.; Buresch, M.; Hartung, R.; Ulm, K., Clinical relevance of urokinase plasminogen activator, its receptor, and its inhibitor in patients with renal cell carcinoma. *Cancer* **1996,** *78* (3), 487-492.

16. Bindal, A. K.; Hammoud, M.; Shi, W. M.; Wu, S. Z.; Sawaya, R.; Rao, J. S., Prognostic significance of proteolytic enzymes in human brain tumors. *Journal of Neuro-Oncology* **1994,** *22* (2), 101-110.

17. Yoo, B.; Pagel, M. D., A PARACEST MRI contrast agent to detect enzyme activity. *Journal of the American Chemical Society* **2006,** *128* (43), 14032-14033.

18. Haftchenary, S.; Luchman, H. A.; Jouk, A. O.; Veloso, A. J.; Page, B. D.; Cheng, X. R.; Dawson, S. S.; Grinshtein, N.; Shahani, V. M.; Kerman, K., Potent targeting of the STAT3 protein in brain cancer stem cells: a promising route for treating glioblastoma. *ACS Medicinal Chemistry Letters* **2013,** *4* (11), 1102-1107.

19. Furlong, S. T.; Mauger, R. C.; Strimpler, A. M.; Liu, Y.-P.; Morris, F. X.; Edwards, P. D., Synthesis and physical characterization of a P_1 arginine combinatorial library, and its application to the determination of the substrate specificity of serine peptidases. *Bioorganic & Medicinal Chemistry* **2002,** *10* (11), 3637-3647.

20. Han, G.; Tamaki, M.; Hruby, V., Fast, efficient and selective deprotection of the tert‐butoxycarbonyl (Boc) group using HCl/dioxane (4 m). *The Journal of Peptide Research* **2001,** *58* (4), 338-341.

21. Bose, D. S.; Lakshminarayana, V., Lewis acid-mediated selective removal of N-tert-butoxycarbonyl protective group (t-Boc). *Synthesis* **1999,** *1999* (1), 66-68.

22. Chen, L. Q.; Randtke, E. A.; Jones, K. M.; Moon, B. F.; Howison, C. M.; Pagel, M. D., Evaluations of tumor acidosis within *in vivo* tumor models using parametric maps generated with acidoCEST MRI. *Molecular Imaging and Biology* **2015,** *17* (4), 488-496.

23. Yoo, B.; Sheth, V. R.; Howison, C. M.; Douglas, M. J.; Pineda, C. T.; Maine, E. A.; Baker, A. F.; Pagel, M. D., Detection of *in vivo* enzyme activity with CatalyCEST MRI. *Magnetic Resonance in Medicine* **2014,** *71* (3), 1221-1230.

24. Sinharay, S.; Howison, C. M.; Baker, A. F.; Pagel, M. D.; Detecting *in vivo* urokinase plasminogen activator activity with a catalyCEST MRI contrast agent. *NMR in Biomedicine* **2017,** *30*(7), 1099-1492.

Chapter 3

FUTURE DIRECTIONS

3.1 Introduction

In this project, we attempted to detect therapeutic response by monitoring uPA activity. However, results showed there was no significant difference between the mice treated with saline and the mice treated with BTZ. The following sections will attempt to address the issues that occurred and improve upon the current study plan.

3.2 Synthesis of Contrast Agent

The current synthesis of the contrast agent is still very tedious and low yielding. An alternative way to approach the synthesis is to use solid phase peptide synthesis. This technique is fast and robust, because the solid support allows for easier purification. Once the peptide is cleaved from the resin, the peptide can be coupled to compound **1**, and the resulting molecule can be deprotected to yield the contrast agent. Wang resin and 2-chlorotrityl chloride resin can be used to produce a carboxylic acid after cleavage from the solid support, which is needed to couple the peptide to the amino group of compound **1**.

The specificity of the peptide chain should also be considered. *In vivo*, uPA cleaves the Arg-Val bond in the sequence CPGR-VVGG of plasminogen to activate plasmin, so many groups have tested similar peptide sequences.[1-4] The established uPA-specific sequences can be conjugated to 4-aminosalicylic acid (para-aminosalicylic acid, PAS) (**Table 3.1**).

Proposed Contrast Agents	
Gly-Gly-Arg-PAS[1]	Glu-Gly-Arg-PAS[2-3]
P2-P1-Arg-PAS[4]	P2-P1-Lys-PAS[4]
P1 = Ala, Gly, Ser, and Thr P2 = Gly, Ser, and Thr	

Table 3.1. *Table of proposed uPA-specific contrast agents with a 4-aminosalicylic acid (PAS) moiety.*

3.3 *In Vivo* Detection of uPA

One way to minimize the biological variation is to perform more precise cell injections into the flank of the mice. The tumors that grew in the mice presented in the previous chapter were not uniform. Some tumors grew very fast and became necrotic, which can be attributed to a highly varied distribution of cells between the injections. Additionally, some of the tumors grew within the muscle tissue and were not truly subcutaneous, which can result in varying biology between tumors. On the other hand, to be more clinically relevant, orthotropic xerographs may be a better approach. These types of tumors can more closely mimic the vasculature and drug accessibility. Other cell lines (e.g., breast, bladder, stomach, etc.) could also be used to see if the change in uPA is more significant in those cell lines.

In this project, only 10 mice were imaged due to the limited material that was synthesized. However, a larger group of mice should be used for better statistical analysis. About 10-12 mice per group (baseline, BTZ-treated, and saline-treated) would be a good starting point. In addition to a larger sample size, more time points can be explored, for instance, 48 h or greater after initiating treatment. Because there was no statistically significant difference between before and after treatment with BTZ scans, the therapy may need more time to decrease the uPA activity. Some other time points that could be investigated are 12 h, 48 h, and/or 72 h post injection. Along the same lines, the dose of BTZ administered could be increased to generate a faster or greater change in uPA activity. However, a standard high dose for mice ranges from 0.5 – 1.0 mg/kg,[5] while in our study, we used 2.0 mg/kg. Alternatively, a different proteasome inhibitor could be injected. Carfilzomib, a more recently FDA approved drug, has been shown to be a successful

substitute for BTZ.[6] Additionally, a longer longitudinal study could be done, where the mice receive a regimen of proteasome inhibitor rather than one injection. Ideally, the gradual decrease of uPA could be monitored though CEST MRI. However, such a study would not allow for meaningful *ex vivo* verification, because several mice need to be sacrificed at every time point for *ex vivo* analysis.

The *ex vivo* analysis remains an integral part of the study because the uPA activity must be validated using an established method. In addition to *ex vivo* measurements of uPA activity of the excised tumors, other venues to be explored are analysis of urine and blood. However, levels of uPA in blood do not necessarily reflect the concentration of uPA in the tumor.[7] In urine, it has been shown that uPA abundance may be correlated with tumor growth.[8] Venues like this are worth exploring in the future because if they are successful, diagnosis of increased uPA activity can be established much faster.

3.4 References for Chapter 3

1. Chung, D. E.; Kratz, F., Development of a novel albumin-binding prodrug that is cleaved by urokinase-type-plasminogen activator (uPA). *Bioorganic & Medicinal Chemistry Letters* **2006,** *16* (19), 5157-5163.

2. Ellis, V.; Wun, T. C.; Behrendt, N.; Rønne, E.; Danø, K., Inhibition of receptor-bound urokinase by plasminogen-activator inhibitors. *Journal of Biological Chemistry* **1990,** *265* (17), 9904-9908.

3. Falkenberg, M.; Tom, C.; DeYoung, M. B.; Wen, S.; Linnemann, R.; Dichek, D. A., Increased expression of urokinase during atherosclerotic lesion development causes arterial constriction and lumen loss, and accelerates lesion growth. *Proceedings of the National Academy of Sciences USA* **2002,** *99* (16), 10665-10670.

4. Gosalia, D. N.; Salisbury, C. M.; Maly, D. J.; Ellman, J. A.; Diamond, S. L., Profiling serine protease substrate specificity with solution phase fluorogenic peptide microarrays. *Proteomics* **2005,** *5* (5), 1292-1298.

5. LeBlanc, R.; Catley, L. P.; Hideshima, T.; Lentzsch, S.; Mitsiades, C. S.; Mitsiades, N.; Neuberg, D.; Goloubeva, O.; Pien, C. S.; Adams, J., Proteasome inhibitor PS-341 inhibits human myeloma cell growth *in vivo* and prolongs survival in a murine model. *Cancer Research* **2002,** *62* (17), 4996-5000.

6. Dimopoulos, M. A.; Moreau, P.; Palumbo, A.; Joshua, D.; Pour, L.; Hájek, R.; Facon, T.; Ludwig, H.; Oriol, A.; Goldschmidt, H., Carfilzomib and dexamethasone versus bortezomib and dexamethasone for patients with relapsed or refractory multiple myeloma (ENDEAVOR): a randomised, phase 3, open-label, multicentre study. *The Lancet Oncology* **2016,** *17* (1), 27-38.

7. Grebenchtchikov, N.; Maguire, T.; Riisbro, R.; Geurts-Moespot, A.; O'Donovan, N.; Schmitt, M.; McGreal, G.; McDermott, E.; O'Higgins, N.; Brünner, N., Measurement of plasminogen activator system components in plasma and tumor tissue extracts obtained from patients with breast cancer: an EORTC Receptor and Biomarker Group collaboration. *Oncology Reports* **2005,** *14* (1), 235-239.

8. Sawaya, R.; Highsmith, R., Plasminogen activator activity and molecular weight patterns in human brain tumors. *Journal of Neurosurgery* **1988,** *68* (1), 73-79.

Appendix A

NMR, MS, AND HPLC SPECTRA

4.1 Compound 1

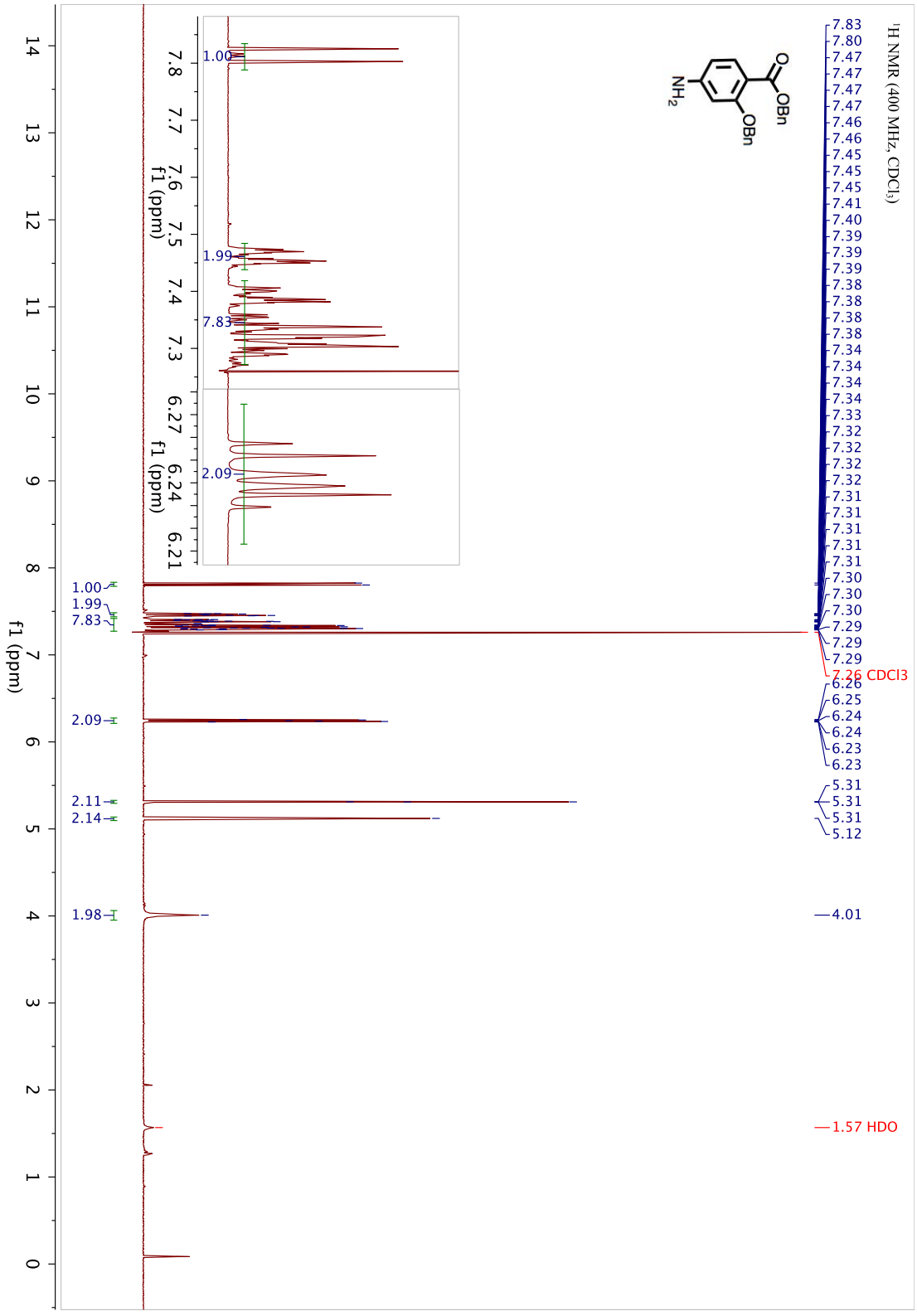

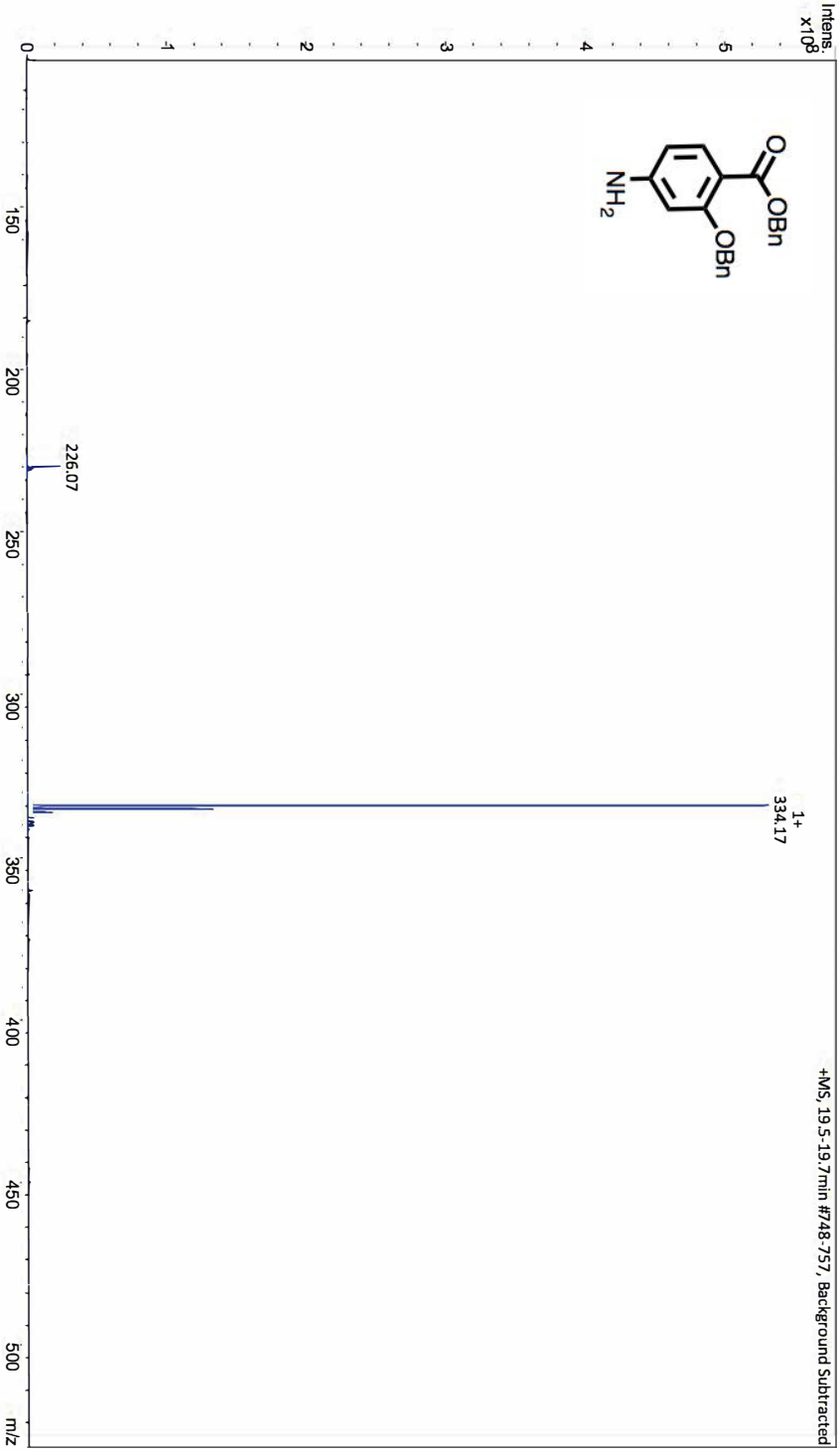
Intens.
x10⁸
5
4
3
2
1
0
150
200
250
300
350
400
450
500
m/z
226.07
1+
334.17
OBn
OBn
NH2
+MS, 19.5-19.7min #748-757, Background Subtracted

4.2 Compound 2

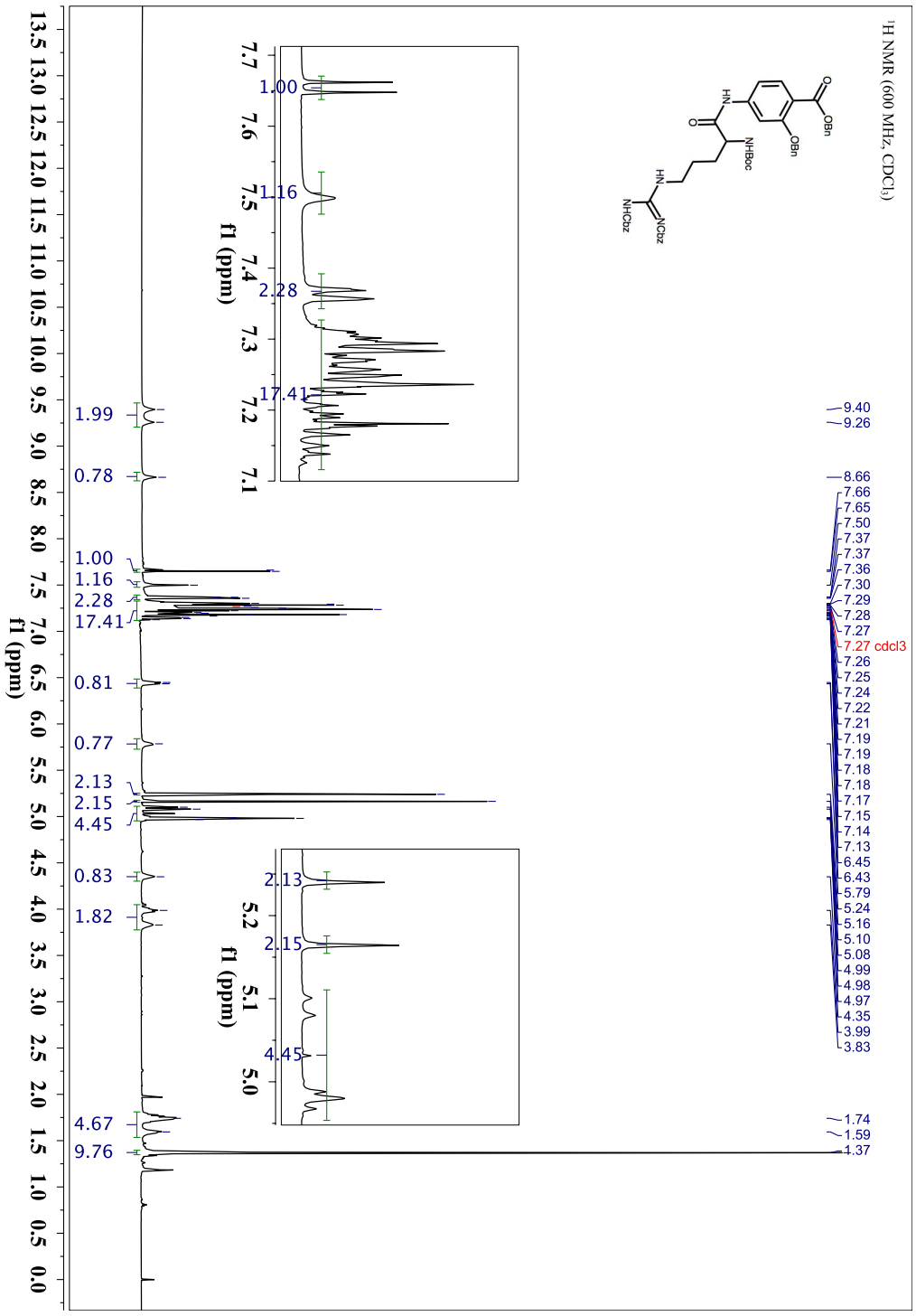

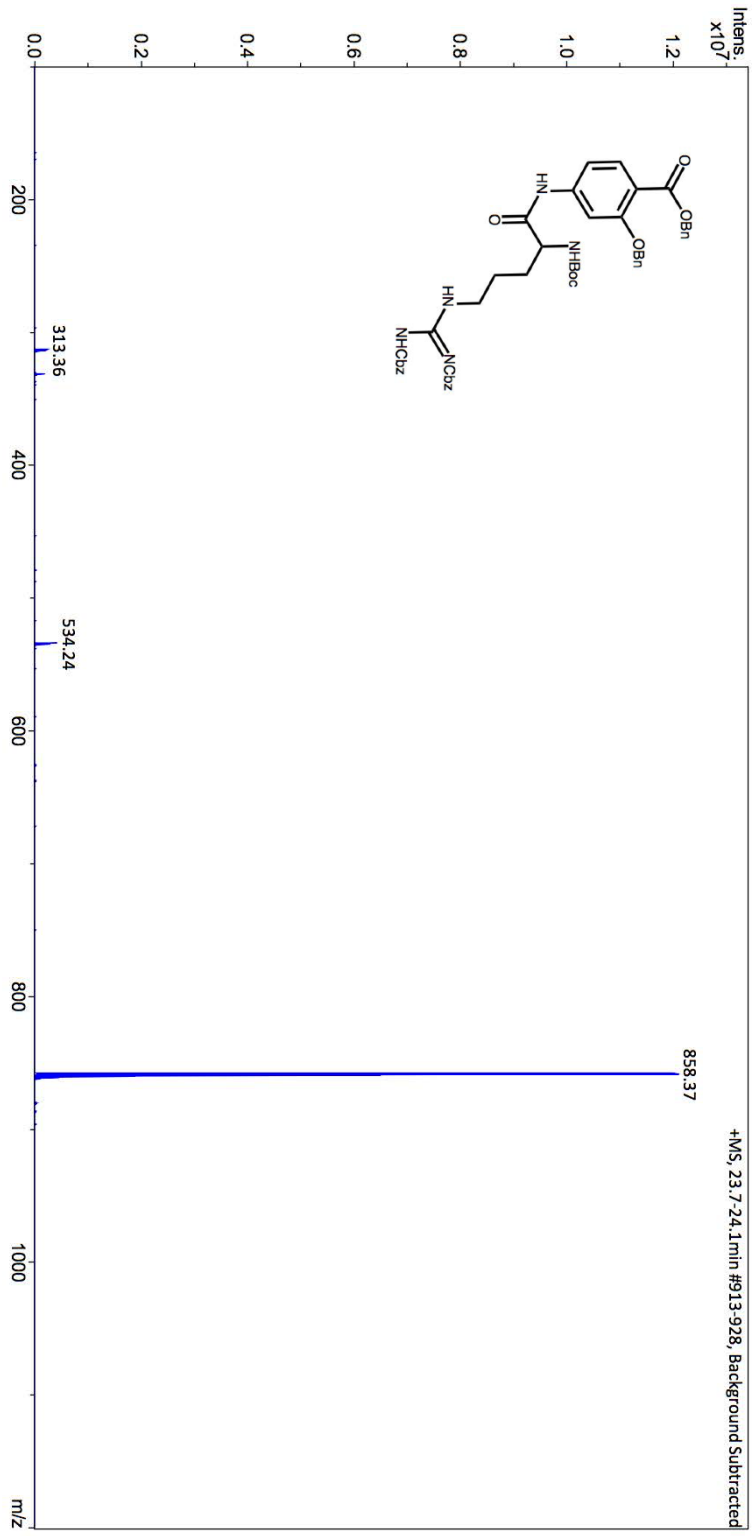
Intens.
x10^7
1.2
1.0
0.8
0.6
0.4
0.2
0.0
200
400
600
800
1000
m/z
313.36
534.24
858.37
+MS, 23.7-24.1min #913-928, Background Subtracted
O
OBn
OBn
HN
O
NHBoc
HN
NCbz
NHCbz

4.3 Compound 3

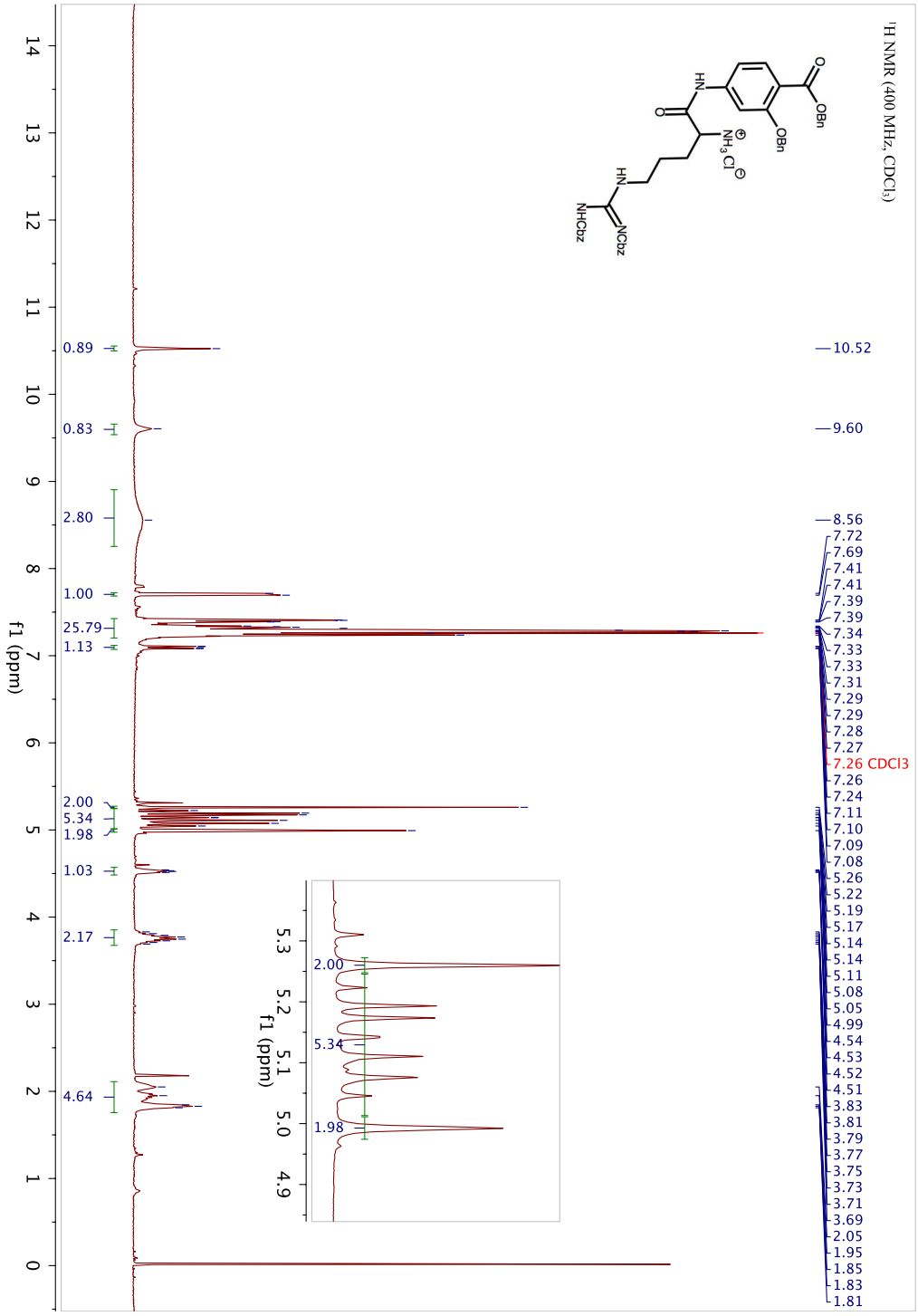

```
=========================================================================
Acq. Operator   : SYSTEM                          Seq. Line :   1
                                                   Location :   93
Injection Date  : 5/1/2017 1:39:47 PM                 Inj :   1
Acq. Method     : KLK6.M
Analysis Method : C:\Chem32\1\Data\Folate-EDBEA 2017-05-01 13-37-36\KLK6.M (Sequence Method)
Last changed    : 5/1/2017 1:37:36 PM by SYSTEM
Sample Info     : Folate-EDBEA
```

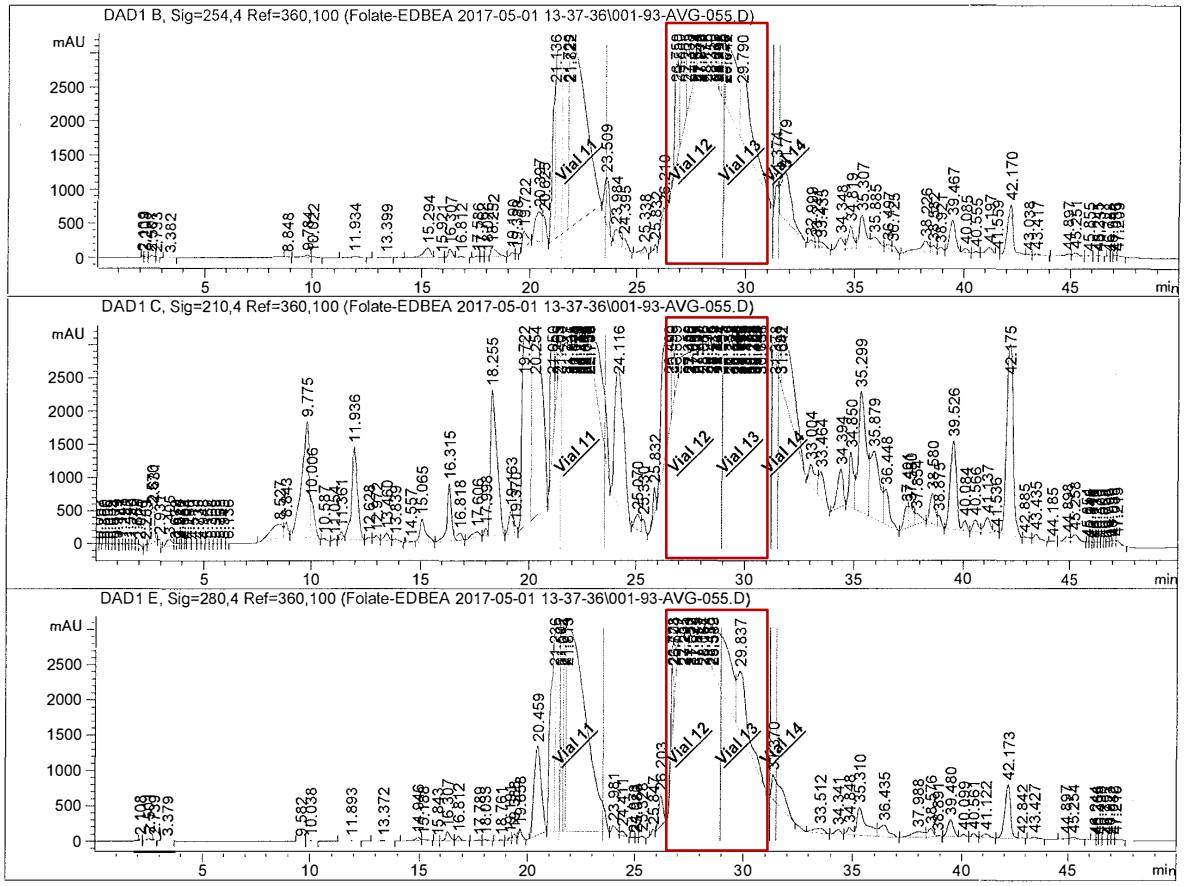

===

4.4 Compound 4

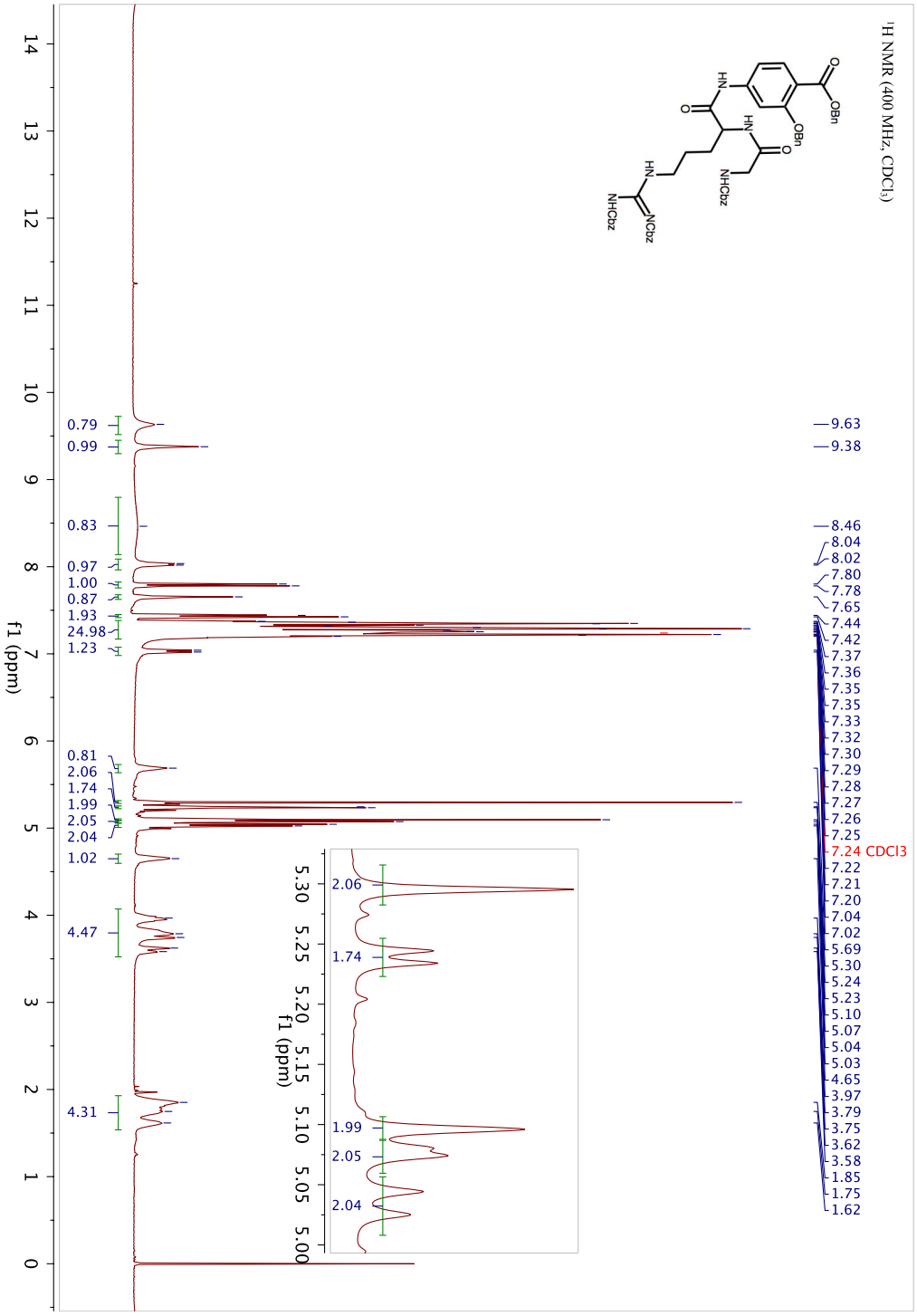

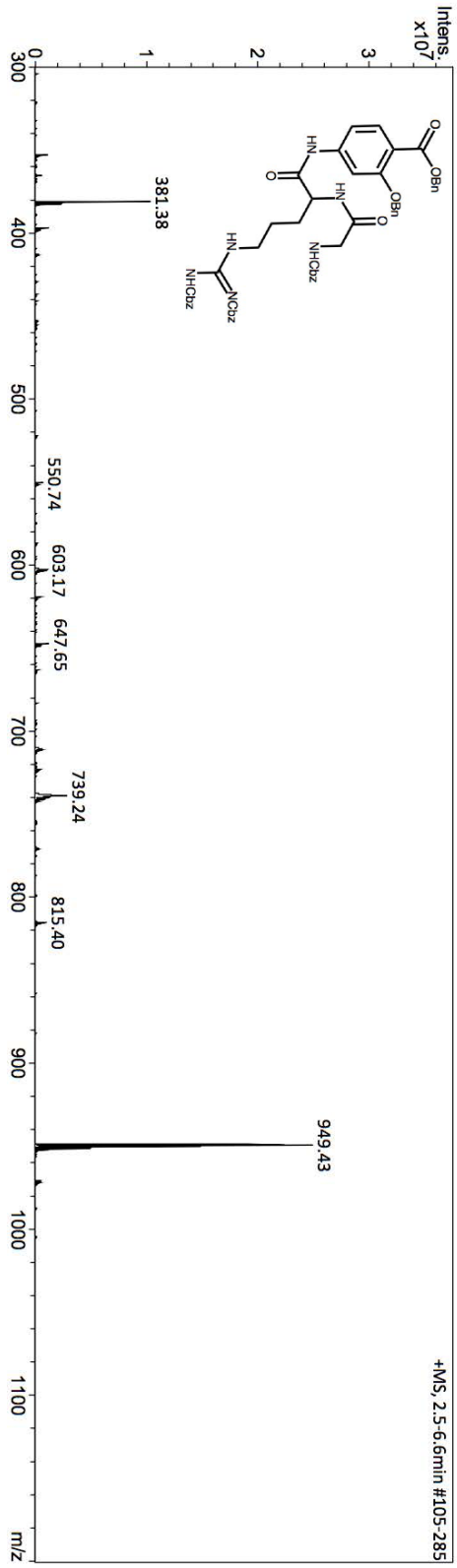
Intens.
x10^7
3
2
1
0
300
400
500
600
700
800
900
1000
1100
m/z
+MS, 2.5-6.6min #105-285
381.38
550.74
603.17
647.65
739.24
815.40
949.43
OBn
OBn
HN
HN
HN
NHCbz
NHCbz
NCbz

```
================================================================================
Acq. Operator   : SYSTEM                          Seq. Line :   1
Acq. Instrument : CAMEL HPLC                     Location :   93
Injection Date  : 5/4/2017 2:06:02 PM                 Inj :   1
                                                 Inj Volume : 500.000 µl
Method          : C:\Chem32\1\Data\Anetta\Folate-EDBEA 2017-05-04 14-04-00\KLK6.M (Sequence
                  Method)
Last changed    : 5/4/2017 2:04:00 PM by SYSTEM
Sample Info     : Folate-EDBEA
```

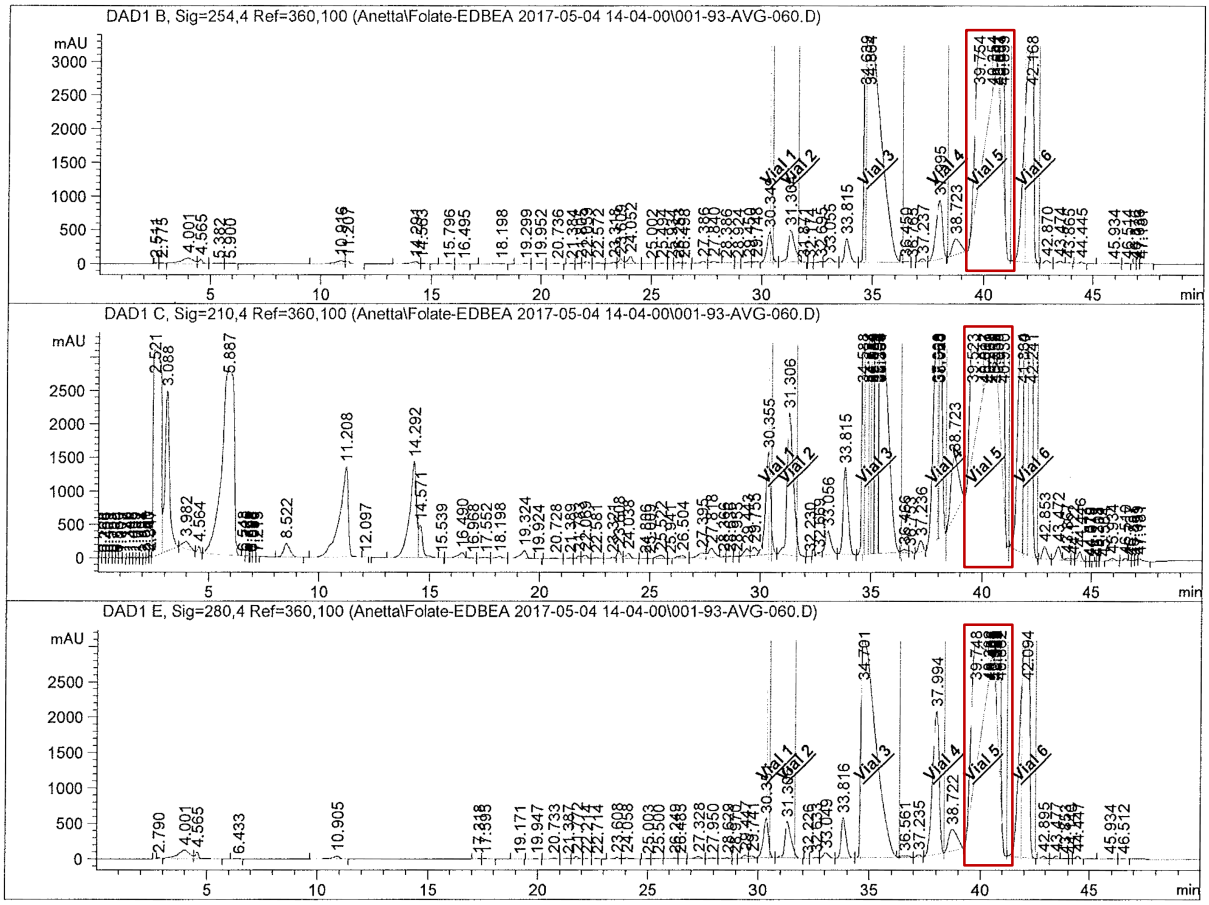


```
================================================================================
```

4.5 Compound 5

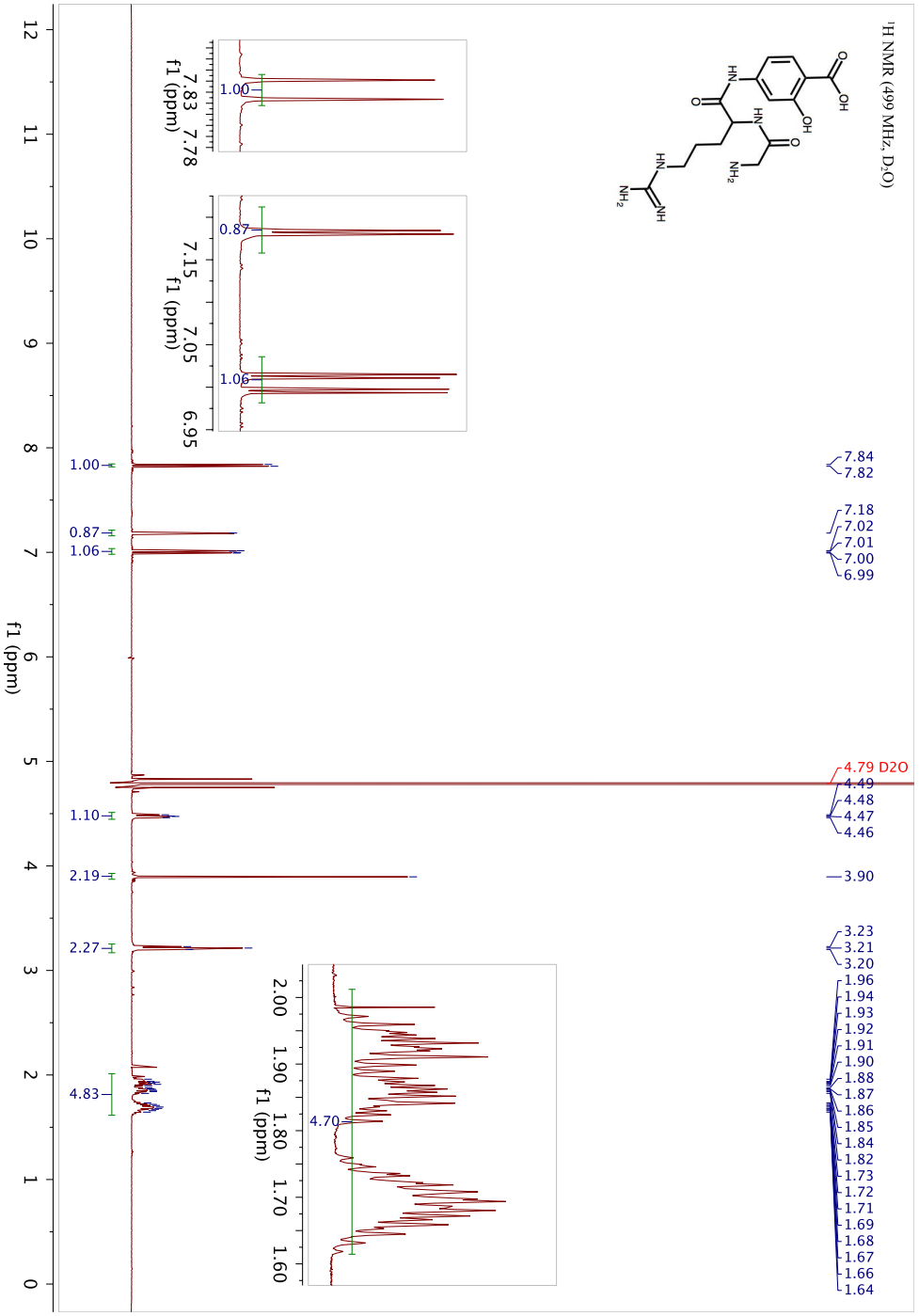

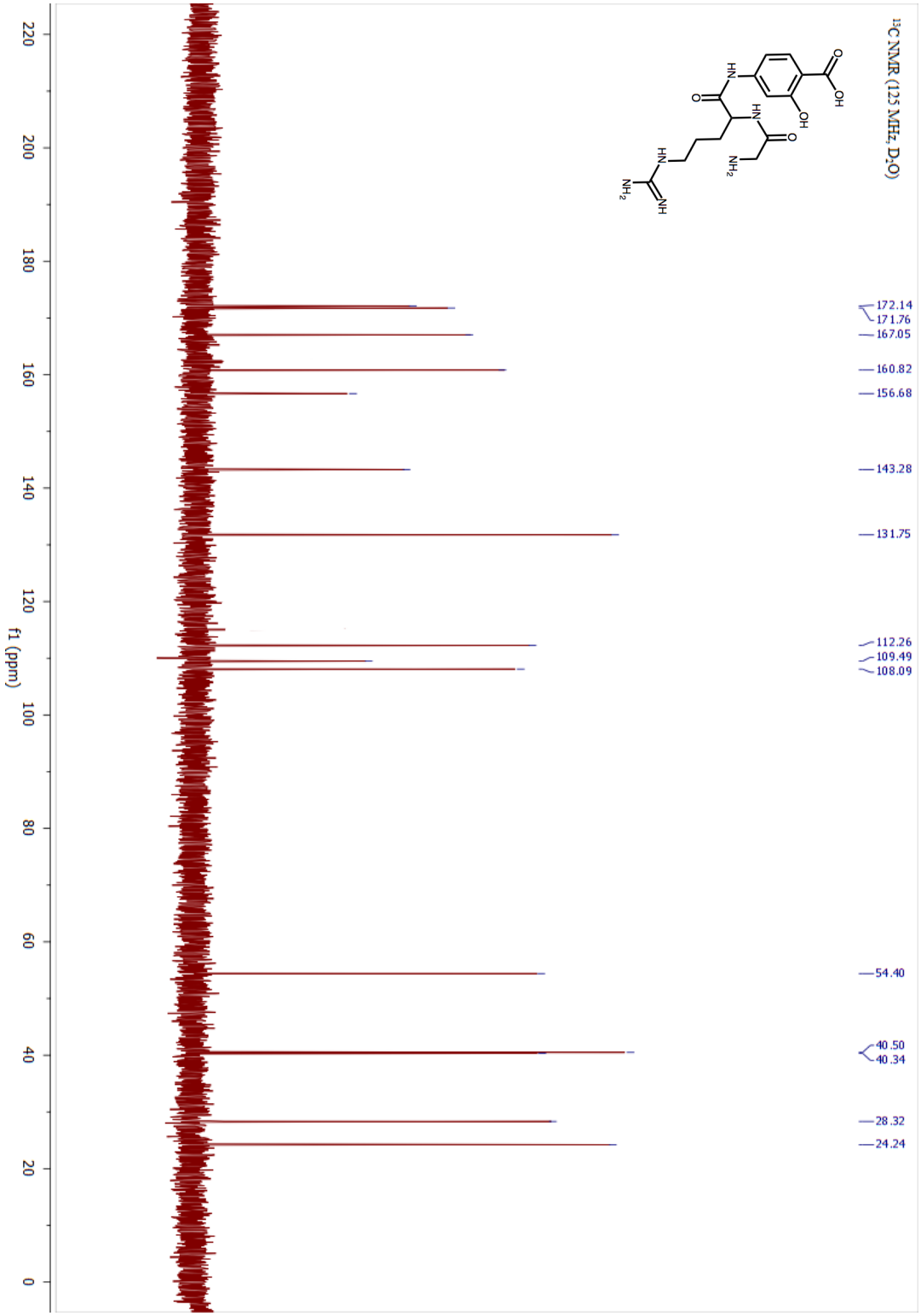
^{13}C NMR (125 MHz, D$_2$O)
172.14
171.76
167.05
160.82
156.68
143.28
131.75
112.26
109.49
108.09
54.40
40.50
40.34
28.32
24.24
f1 (ppm)
0
20
40
60
80
100
120
140
160
180
200
220

Acquisition Parameter

Polarity	Positive	Source	ESI	No. of Laser Shots	20
Averaged Scans	20	No. of Cell Fills	1	Laser Power	51.0 %
Broadband Low Mass	57.7 m/z	End Plate	3500.0 V	MALDI Plate	230.0 V
Broadband High Mass	800.0 m/z	Capillary Entrance	4200.0 V	Imaging Spot Diameter	2000.0 µm
Acquisition Mode	Single MS	Skimmer 1	32.0 V		
Pulse Program	BASIC	Drying Gas Temperature	200.0 °C	Calibration Date	Thu Jun 1 01:39:32 2017
Source Accumulation	0.1 sec	Drying Gas Flow Rate	2.5 L/min	Data Acquisition Size	1048576
Ion Accumulation Time	0.4 sec	Nebulizer Gas Flow Rate	1.5 L/min	Apodization	Square Sine-Bell Multiplication
Flight Time to Acq. Cell	0.0 sec				

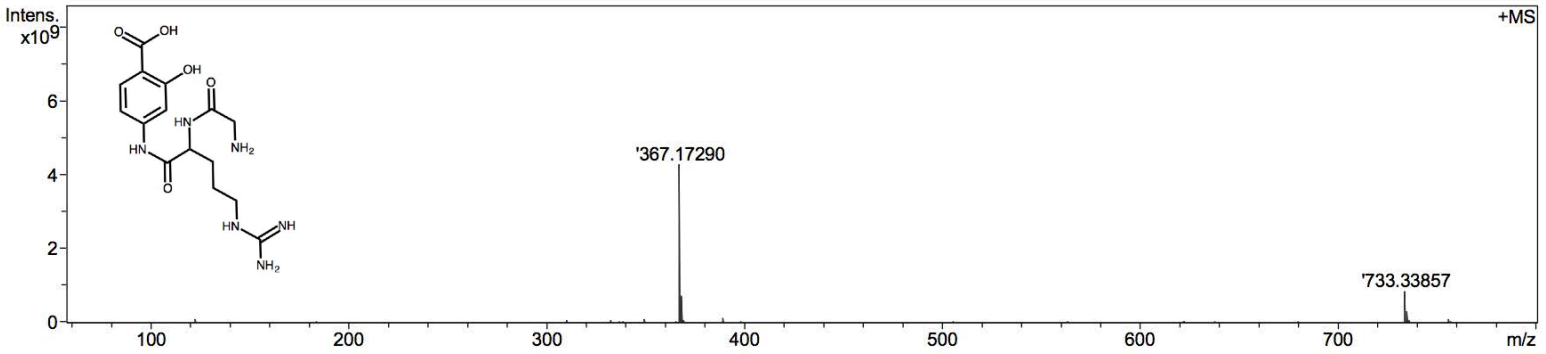

Meas. m/z	Formula	m/z	err [ppm]	mSigma	Std Comb Dev
367.17290					
	C 15 H 23 N 6 O 5	367.17244	-1.2	107.53	0.8427

```
==========================================================================
Acq. Operator   : SYSTEM                          Seq. Line :   1
Acq. Instrument : CAMEL HPLC                      Location :   93
Injection Date  : 5/12/2017 2:56:41 PM                Inj :   1
                                                Inj Volume : 500.000 µl
Method          : C:\Chem32\1\Data\Anetta\Folate-EDBEA 2017-05-12 14-54-45\AVG-Compound5.M (
                  Sequence Method)
Last changed    : 5/12/2017 2:54:45 PM by SYSTEM
Sample Info     : Folate-EDBEA
```

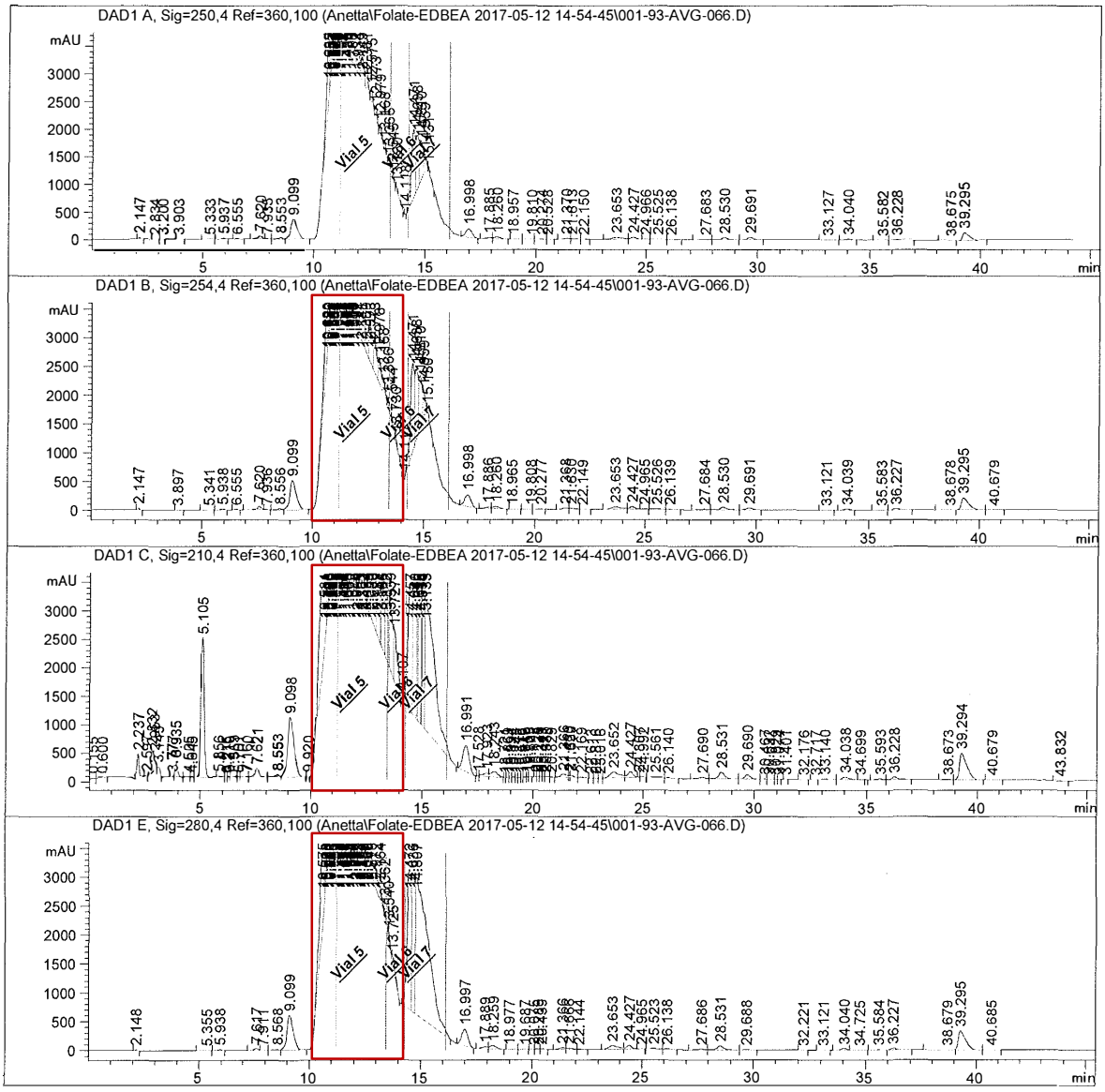

==========

Comprehensive List of References

References for Chapter 1

1. Baruch, A.; Jeffery, D. A.; Bogyo, M., Enzyme activity–it's all about image. *Trends in Cell Biology* **2004,** *14* (1), 29-35.

2. Kobayashi, H.; Choyke, P. L., Target-cancer-cell-specific activatable fluorescence imaging probes: rational design and *in vivo* applications. *Accounts of Chemical Research* **2010,** *44* (2), 83-90.

3. Razgulin, A.; Ma, N.; Rao, J., Strategies for *in vivo* imaging of enzyme activity: an overview and recent advances. *Chemical Society Reviews* **2011,** *40* (7), 4186-4216.

4. Kobayashi, H.; Ogawa, M.; Alford, R.; Choyke, P. L.; Urano, Y., New strategies for fluorescent probe design in medical diagnostic imaging. *Chemical Reviews* **2009,** *110* (5), 2620-2640.

5. Ntziachristos, V.; Razansky, D., Molecular imaging by means of multispectral optoacoustic tomography (MSOT). *Chemical Reviews* **2010,** *110* (5), 2783-2794.

6. Yan, R.; Ye, D., Molecular imaging of enzyme activity *in vivo* using activatable probes. *Science Bulletin* **2016,** *61* (21), 1672-1679.

7. Massoud, T. F.; Gambhir, S. S., Molecular imaging in living subjects: seeing fundamental biological processes in a new light. *Genes & Development* **2003,** *17* (5), 545-580.

8. Kamiya, M.; Urano, Y., Rapid and sensitive fluorescent imaging of tiny tumors *in vivo* and in clinical specimens. *Current Opinion in Chemical Biology* **2016,** *33*, 9-15.

9. Van Dam, G. M.; Themelis, G.; Crane, L. M.; Harlaar, N. J.; Pleijhuis, R. G.; Kelder, W.; Sarantopoulos, A.; De Jong, J. S.; Arts, H. J.; Van Der Zee, A. G., Intraoperative tumor-specific fluorescence imaging in ovarian cancer by folate receptor-α targeting: first in-human results. *Nature Medicine* **2011,** *17* (10), 1315-1319.

10. Kikuchi, K., Design, synthesis and biological application of chemical probes for bio-imaging. *Chemical Society Reviews* **2010,** *39* (6), 2048-2053.

11. Jiang, S.; Win, K. Y.; Liu, S.; Teng, C. P.; Zheng, Y.; Han, M.-Y., Surface-functionalized nanoparticles for biosensing and imaging-guided therapeutics. *Nanoscale* **2013,** *5* (8), 3127-3148.

12. Lakowicz, J. R., Introduction to fluorescence. In *Principles of Fluorescence Spectroscopy*, Springer: 1999; pp 1-23.

13. Tsien, R.; Harootunian, A., Practical design criteria for a dynamic ratio imaging system. *Cell Calcium* **1990,** *11* (2-3), 93-109.

14. Ntziachristos, V.; Ripoll, J.; Weissleder, R., Would near-infrared fluorescence signals propagate through large human organs for clinical studies? *Optics Letters* **2002,** *27* (5), 333-335.

15. Ntziachristos, V.; Bremer, C.; Weissleder, R., Fluorescence imaging with near-infrared light: new technological advances that enable *in vivo* molecular imaging. *European Radiology* **2003,** *13* (1), 195-208.

16. Smith, K., *The Science of Photobiology*. Springer Science & Business Media: 2013.

17. Thorne, S. H.; Barak, Y.; Liang, W.; Bachmann, M. H.; Rao, J.; Contag, C. H.; Matin, A., CNOB/ChrR6, a new prodrug enzyme cancer chemotherapy. *Molecular Cancer Therapeutics* **2009,** *8* (2), 333-341.

18. Versluis, F.; van Esch, J. H.; Eelkema, R., Synthetic self‐assembled materials in biological environments. *Advanced Materials* **2016,** *28* (23), 4576-4592.

19. Ye, D.; Shuhendler, A. J.; Cui, L.; Tong, L.; Tee, S. S.; Tikhomirov, G.; Felsher, D. W.; Rao, J., Bioorthogonal cyclization-mediated *in situ* self-assembly of small-molecule probes for imaging caspase activity *in vivo*. *Nature Chemistry* **2014,** *6* (6), 519-526.

20. Wolfbeis, O. S., An overview of nanoparticles commonly used in fluorescent bioimaging. *Chemical Society Reviews* **2015,** *44* (14), 4743-4768.

21. Gao, X.; Yang, L.; Petros, J. A.; Marshall, F. F.; Simons, J. W.; Nie, S., *In vivo* molecular and cellular imaging with quantum dots. *Current Opinion in Biotechnology* **2005,** *16* (1), 63-72.

22. Michalet, X.; Pinaud, F.; Bentolila, L.; Tsay, J.; Doose, S.; Li, J.; Sundaresan, G.; Wu, A.; Gambhir, S.; Weiss, S., Quantum dots for live cells, *in vivo* imaging, and diagnostics. *Science* **2005,** *307* (5709), 538-544.

23. Rao, J.; Dragulescu-Andrasi, A.; Yao, H., Fluorescence imaging *in vivo*: recent advances. *Current Opinion in Biotechnology* **2007,** *18* (1), 17-25.

24. Frangioni, J. V., *In vivo* near-infrared fluorescence imaging. *Current Opinion in Chemical Biology* **2003,** *7* (5), 626-634.

25. Li, X.; Deng, D.; Xue, J.; Qu, L.; Achilefu, S.; Gu, Y., Quantum dots based molecular beacons for *in vitro* and *in vivo* detection of MMP-2 on tumor. *Biosensors and Bioelectronics* **2014,** *61*, 512-518.

26. Lee, S.; Ryu, J. H.; Park, K.; Lee, A.; Lee, S.-Y.; Youn, I.-C.; Ahn, C.-H.; Yoon, S. M.; Myung, S.-J.; Moon, D. H., Polymeric nanoparticle-based activatable near-infrared nanosensor for protease determination *in vivo*. *Nano Letters* **2009,** *9* (12), 4412-4416.

27. Weissleder, R.; Tung, C.-H.; Mahmood, U.; Bogdanov, A., *In vivo* imaging of tumors with protease-activated near-infrared fluorescent probes. *Nature Biotechnology* **1999,** *17* (4), 375-378.

28. Hsiao, J.-K.; Law, B.; Weissleder, R.; Tung, C.-H., *In-vivo* imaging of tumor associated urokinase-type plasminogen activator activity. *Journal of Biomedical Optics* **2006,** *11* (3), 034013-034013-5.

29. Thorne, N.; Inglese, J.; Auld, D. S., Illuminating insights into firefly luciferase and other bioluminescent reporters used in chemical biology. *Chemistry & Biology* **2010,** *17* (6), 646-657.

30. Dragulescu-Andrasi, A.; Liang, G.; Rao, J., *In vivo* bioluminescence imaging of furin activity in breast cancer cells using bioluminogenic substrates. *Bioconjugate Chemistry* **2009,** *20* (8), 1660-1666.

31. Yao, H.; So, M. K.; Rao, J., A bioluminogenic substrate for *in vivo* imaging of β‐lactamase activity. *Angewandte Chemie International Edition* **2007,** *46* (37), 7031-7034.

32. Wehrman, T. S.; von Degenfeld, G.; Krutzik, P. O.; Nolan, G. P.; Blau, H. M., Luminescent imaging of β-galactosidase activity in living subjects using sequential reporter-enzyme luminescence. *Nature Methods* **2006,** *3* (4), 295-301.

33. Kanno, A.; Yamanaka, Y.; Hirano, H.; Umezawa, Y.; Ozawa, T., Cyclic luciferase for real‐time sensing of caspase‐3 activities in living mammals. *Angewandte Chemie International Edition* **2007,** *46* (40), 7595-7599.

34. Laxman, B.; Hall, D. E.; Bhojani, M. S.; Hamstra, D. A.; Chenevert, T. L.; Ross, B. D.; Rehemtulla, A., Noninvasive real-time imaging of apoptosis. *Proceedings of the National Academy of Sciences USA* **2002,** *99* (26), 16551-16555.

35. Davies, G.-L.; Kramberger, I.; Davis, J. J., Environmentally responsive MRI contrast agents. *Chemical Communications* **2013,** *49* (84), 9704-9721.

36. Hingorani, D. V.; Yoo, B.; Bernstein, A. S.; Pagel, M. D., Detecting enzyme activities with exogenous MRI contrast agents. *Chemistry–A European Journal* **2014,** *20* (32), 9840-9850.

37. Louie, A. Y.; Hüber, M. M.; Ahrens, E. T.; Rothbächer, U.; Moats, R.; Jacobs, R. E.; Fraser, S. E.; Meade, T. J., *In vivo* visualization of gene expression using magnetic resonance imaging. *Nature Biotechnology* **2000,** *18* (3), 321-325.

38. Chang, Y.-T.; Cheng, C.-M.; Su, Y.-Z.; Lee, W.-T.; Hsu, J.-S.; Liu, G.-C.; Cheng, T.-L.; Wang, Y.-M., Synthesis and characterization of a new bioactivated paramagnetic gadolinium (III) complex [Gd (DOTA-FPG)(H2O)] for tracing gene expression. *Bioconjugate Chemistry* **2007,** *18* (6), 1716-1727.

39. Rodríguez, E.; Nilges, M.; Weissleder, R.; Chen, J. W., Activatable magnetic resonance imaging agents for myeloperoxidase sensing: mechanism of activation, stability, and toxicity. *Journal of the American Chemical Society* **2009,** *132* (1), 168-177.

40. Yoo, B.; Pagel, M. D., An overview of responsive MRI contrast agents for molecular imaging. *Frontiers in Bioscience: A Journal and Virtual Library* **2007,** *13*, 1733-1752.

41. Hingorani, D. V.; Bernstein, A. S.; Pagel, M. D., A review of responsive MRI contrast agents: 2005–2014. *Contrast Media & Molecular Imaging* **2015,** *10* (4), 245-265.

42. Granot, D.; Shapiro, E. M., Release activation of iron oxide nanoparticles:(REACTION) a novel environmentally sensitive MRI paradigm. *Magnetic Resonance in Medicine* **2011,** *65* (5), 1253-1259.

43. Colomb, J.; Louie, K.; Massia, S. P.; Bennett, K. M., Self‐degrading, MRI‐detectable hydrogel sensors with picomolar target sensitivity. *Magnetic Resonance in Medicine* **2010,** *64* (6), 1792-1799.

44. Hingorani, D. V.; Montano, L. A.; Randtke, E. A.; Lee, Y. S.; Cárdenas‐Rodríguez, J.; Pagel, M. D., A single diamagnetic catalyCEST MRI contrast agent that detects cathepsin B enzyme activity by using a ratio of two CEST signals. *Contrast Media & Molecular Imaging* **2016,** *11* (2), 130-138.

45. Sinharay, S.; Randtke, E. A.; Jones, K. M.; Howison, C. M.; Chambers, S. K.; Kobayashi, H.; Pagel, M. D., Noninvasive detection of enzyme activity in tumor models of human ovarian cancer using catalyCEST MRI. *Magnetic Resonance in Medicine* **2017,** *77* (5), 2005-2014.

46. Yoo, B.; Sheth, V. R.; Howison, C. M.; Douglas, M. J.; Pineda, C. T.; Maine, E. A.; Baker, A. F.; Pagel, M. D., Detection of *in vivo* enzyme activity with CatalyCEST MRI. *Magnetic Resonance in Medicine* **2014,** *71* (3), 1221-1230.

47. Ametamey, S. M.; Honer, M.; Schubiger, P. A., Molecular imaging with PET. *Chemical Reviews* **2008,** *108* (5), 1501-1516.

48. Couturier, O.; Luxen, A.; Chatal, J.-F.; Vuillez, J.-P.; Rigo, P.; Hustinx, R., Fluorinated tracers for imaging cancer with positron emission tomography. *European Journal of Nuclear Medicine and Molecular Imaging* **2004,** *31* (8), 1182-1206.

49. Smith, T., FDG uptake, tumour characteristics and response to therapy: a review. *Nuclear Medicine Communications* **1998,** *19* (2), 97-106.

50. Tjuvajev, J. G.; Finn, R.; Watanabe, K.; Joshi, R.; Oku, T.; Kennedy, J.; Beattie, B.; Koutcher, J.; Larson, S.; Blasberg, R. G., Noninvasive imaging of herpes virus thymidine

kinase gene transfer and expression: a potential method for monitoring clinical gene therapy. *Cancer Research* **1996,** *56* (18), 4087-4095.

51. Lee, K.-H.; Byun, S. S.; Choi, J. H.; Paik, J.-Y.; Choe, Y. S.; Kim, B.-T., Targeting of lacZ reporter gene expression with radioiodine-labelled phenylethyl-β-d-thiogalactopyranoside. *European Journal of Nuclear Medicine and Molecular Imaging* **2004,** *31* (3), 433-438.

52. Zhou, D.; Chu, W.; Rothfuss, J.; Zeng, C.; Xu, J.; Jones, L.; Welch, M. J.; Mach, R. H., Synthesis, radiolabeling, and *in vivo* evaluation of an 18F-labeled isatin analog for imaging caspase-3 activation in apoptosis. *Bioorganic & Medicinal Chemistry Letters* **2006,** *16* (19), 5041-5046.

53. Su, J. L.; Wang, B.; Wilson, K. E.; Bayer, C. L.; Chen, Y.-S.; Kim, S.; Homan, K. A.; Emelianov, S. Y., Advances in clinical and biomedical applications of photoacoustic imaging. *Expert Opinion on Medical Diagnostics* **2010,** *4* (6), 497-510.

54. Kim, C.; Favazza, C.; Wang, L. V., *In vivo* photoacoustic tomography of chemicals: high-resolution functional and molecular optical imaging at new depths. *Chemical Reviews* **2010,** *110* (5), 2756-2782.

55. Li, L.; Zemp, R. J.; Lungu, G.; Stoica, G.; Wang, L. V., Photoacoustic imaging of lacZ gene expression *in vivo*. *Journal of Biomedical Optics* **2007,** *12* (2), 020504-020504-3.

56. Levi, J.; Kothapalli, S. R.; Ma, T.-J.; Hartman, K.; Khuri-Yakub, B. T.; Gambhir, S. S., Design, synthesis, and imaging of an activatable photoacoustic probe. *Journal of the American Chemical Society* **2010,** *132* (32), 11264-11269.

57. Wang, L.; Yang, P.-P.; Zhao, X.-X.; Wang, H., Self-assembled nanomaterials for photoacoustic imaging. *Nanoscale* **2016,** *8* (5), 2488-2509.

58. Dragulescu-Andrasi, A.; Kothapalli, S.-R.; Tikhomirov, G. A.; Rao, J.; Gambhir, S. S., Activatable oligomerizable imaging agents for photoacoustic imaging of furin-like activity in living subjects. *Journal of the American Chemical Society* **2013,** *135* (30), 11015-11022.

59. Zhang, D.; Qi, G. B.; Zhao, Y. X.; Qiao, S. L.; Yang, C.; Wang, H., *In situ* formation of nanofibers from purpurin18‐peptide conjugates and the assembly induced retention effect in tumor sites. *Advanced Materials* **2015,** *27* (40), 6125-6130.

References for Chapter 2

1. McKay, L. I.; Cidlowski, J. A., Molecular control of immune/inflammatory responses: interactions between nuclear factor-κB and steroid receptor-signaling pathways. *Endocrine Reviews* **1999,** *20* (4), 435-459.

2. Andela, V. B.; Schwarz, E. M.; Puzas, J. E.; O'Keefe, R. J.; Rosier, R. N., Tumor metastasis and the reciprocal regulation of prometastatic and antimetastatic factors by nuclear factor κB. *Cancer Research* **2000,** *60* (23), 6557-6562.

3. Crippa, M. P., Urokinase-type plasminogen activator. *The International Journal of Biochemistry & Cell Biology* **2007,** *39* (4), 690-694.

4. Das, R.; Philip, S.; Mahabeleshwar, G. H.; Bulbule, A.; Kundu, G. C., Osteopontin: it's role in regulation of cell motility and nuclear factor κB‐mediated urokinase type plasminogen activator expression. *IUBMB Life* **2005,** *57* (6), 441-447.

5. Mekkawy, A. H.; Pourgholami, M. H.; Morris, D. L., Involvement of urokinase‐type plasminogen activator system in cancer: an overview. *Medicinal Research Reviews* **2014,** *34* (5), 918-956.

6. Andreasen, P. A.; Kjøller, L.; Christensen, L.; Duffy, M. J., The urokinase‐type plasminogen activator system in cancer metastasis: a review. *International Journal of Cancer* **1997,** *72* (1), 1-22.

7. Wang, Y., The role and regulation of urokinase‐type plasminogen activator receptor gene expression in cancer invasion and metastasis. *Medicinal Research Reviews* **2001,** *21* (2), 146-170.

8. Duffy, M. J.; O'Siorain, L.; O'Grady, P.; Devaney, D.; Fennelly, J. J.; Lijnen, H. J., Urokinase‐plasminogen activator, a marker for aggressive breast carcinomas. Preliminary report. *Cancer* **1988,** *62* (3), 531-533.

9. Oka, T.; Ishida, T.; Nishino, T.; Sugimachi, K., Immunohistochemical evidence of urokinase-type plasminogen activator in primary and metastatic tumors of pulmonary adenocarcinoma. *Cancer Research* **1991,** *51* (13), 3522-3525.

10. Hasui, Y.; Marutsuka, K.; Suzumiya, J.; Kitada, S.; Osada, Y.; Sumiyoshi, A., The content of urokinase‐type plasminogen activator antigen as a prognostic factor in urinary bladder cancer. *International Journal of Cancer* **1992,** *50* (6), 871-873.

11. Nekarda, H.; Siewert, J.; Schmitt, M.; Ulm, K., Tumour-associated proteolytic factors uPA and PAI-1 and survival in totally resected gastric cancer. *The Lancet* **1994,** *343* (8889), 117.

12. Mulcahy, H.; O'Donoghue, D.; Duffy, M.; Gibbons, D.; McCarthy, P.; Parfrey, N.; Sheahan, K., Urokinase-type plasminogen activator and outcome in Dukes' B colorectal cancer. *The Lancet* **1994,** *344* (8922), 583-584.

13. Kobayashi, H.; Fujishiro, S.; Terao, T., Impact of urokinase-type plasminogen activator and its inhibitor type 1 on prognosis in cervical cancer of the uterus. *Cancer Research* **1994,** *54* (24), 6539-6548.

14. Kuhn, W.; Pache, L.; Schmalfeldt, B.; Dettmar, P.; Schmitt, M.; Jänicke, F.; Graeff, H., Urokinase (uPA) and PAI-1 predict survival in advanced ovarian cancer patients (FIGO III) after radical surgery and platinum-based chemotherapy. *Gynecologic Oncology* **1994,** *55* (3), 401-409.

15. Hofmann, R.; Lehmer, A.; Buresch, M.; Hartung, R.; Ulm, K., Clinical relevance of urokinase plasminogen activator, its receptor, and its inhibitor in patients with renal cell carcinoma. *Cancer* **1996,** *78* (3), 487-492.

16. Bindal, A. K.; Hammoud, M.; Shi, W. M.; Wu, S. Z.; Sawaya, R.; Rao, J. S., Prognostic significance of proteolytic enzymes in human brain tumors. *Journal of Neuro-Oncology* **1994,** *22* (2), 101-110.

17. Yoo, B.; Pagel, M. D., A PARACEST MRI contrast agent to detect enzyme activity. *Journal of the American Chemical Society* **2006,** *128* (43), 14032-14033.

18. Haftchenary, S.; Luchman, H. A.; Jouk, A. O.; Veloso, A. J.; Page, B. D.; Cheng, X. R.; Dawson, S. S.; Grinshtein, N.; Shahani, V. M.; Kerman, K., Potent targeting of the STAT3 protein in brain cancer stem cells: a promising route for treating glioblastoma. *ACS Medicinal Chemistry Letters* **2013,** *4* (11), 1102-1107.

19. Furlong, S. T.; Mauger, R. C.; Strimpler, A. M.; Liu, Y.-P.; Morris, F. X.; Edwards, P. D., Synthesis and physical characterization of a P_1 arginine combinatorial library, and its application to the determination of the substrate specificity of serine peptidases. *Bioorganic & Medicinal Chemistry* **2002,** *10* (11), 3637-3647.

20. Han, G.; Tamaki, M.; Hruby, V., Fast, efficient and selective deprotection of the tert‐butoxycarbonyl (Boc) group using HCl/dioxane (4 m). *The Journal of Peptide Research* **2001,** *58* (4), 338-341.

21. Bose, D. S.; Lakshminarayana, V., Lewis acid-mediated selective removal of N-tert-butoxycarbonyl protective group (t-Boc). *Synthesis* **1999,** *1999* (1), 66-68.

22. Chen, L. Q.; Randtke, E. A.; Jones, K. M.; Moon, B. F.; Howison, C. M.; Pagel, M. D., Evaluations of tumor acidosis within *in vivo* tumor models using parametric maps generated with acidoCEST MRI. *Molecular Imaging and Biology* **2015,** *17* (4), 488-496.

23. Yoo, B.; Sheth, V. R.; Howison, C. M.; Douglas, M. J.; Pineda, C. T.; Maine, E. A.; Baker, A. F.; Pagel, M. D., Detection of *in vivo* enzyme activity with CatalyCEST MRI. *Magnetic Resonance in Medicine* **2014,** *71* (3), 1221-1230.

References for Chapter 3

1. Chung, D. E.; Kratz, F., Development of a novel albumin-binding prodrug that is cleaved by urokinase-type-plasminogen activator (uPA). *Bioorganic & Medicinal Chemistry Letters* **2006,** *16* (19), 5157-5163.

2. Ellis, V.; Wun, T. C.; Behrendt, N.; Rønne, E.; Danø, K., Inhibition of receptor-bound urokinase by plasminogen-activator inhibitors. *Journal of Biological Chemistry* **1990,** *265* (17), 9904-9908.

3. Falkenberg, M.; Tom, C.; DeYoung, M. B.; Wen, S.; Linnemann, R.; Dichek, D. A., Increased expression of urokinase during atherosclerotic lesion development causes arterial constriction and lumen loss, and accelerates lesion growth. *Proceedings of the National Academy of Sciences USA* **2002,** *99* (16), 10665-10670.

4. Gosalia, D. N.; Salisbury, C. M.; Maly, D. J.; Ellman, J. A.; Diamond, S. L., Profiling serine protease substrate specificity with solution phase fluorogenic peptide microarrays. *Proteomics* **2005,** *5* (5), 1292-1298.

5. LeBlanc, R.; Catley, L. P.; Hideshima, T.; Lentzsch, S.; Mitsiades, C. S.; Mitsiades, N.; Neuberg, D.; Goloubeva, O.; Pien, C. S.; Adams, J., Proteasome inhibitor PS-341 inhibits human myeloma cell growth *in vivo* and prolongs survival in a murine model. *Cancer Research* **2002,** *62* (17), 4996-5000.

6. Dimopoulos, M. A.; Moreau, P.; Palumbo, A.; Joshua, D.; Pour, L.; Hájek, R.; Facon, T.; Ludwig, H.; Oriol, A.; Goldschmidt, H., Carfilzomib and dexamethasone versus bortezomib and dexamethasone for patients with relapsed or refractory multiple myeloma (ENDEAVOR): a randomised, phase 3, open-label, multicentre study. *The Lancet Oncology* **2016,** *17* (1), 27-38.

7. Grebenchtchikov, N.; Maguire, T.; Riisbro, R.; Geurts-Moespot, A.; O'Donovan, N.; Schmitt, M.; McGreal, G.; McDermott, E.; O'Higgins, N.; Brünner, N., Measurement of plasminogen activator system components in plasma and tumor tissue extracts obtained from patients with breast cancer: an EORTC Receptor and Biomarker Group collaboration. *Oncology Reports* **2005,** *14* (1), 235-239.

8. Sawaya, R.; Highsmith, R., Plasminogen activator activity and molecular weight patterns in human brain tumors. *Journal of Neurosurgery* **1988,** *68* (1), 73-79.